Department of Applied Physics

Modelling of global impurity transport in tokamaks in the presence of non-axisymmetric effects

Juho Miettunen

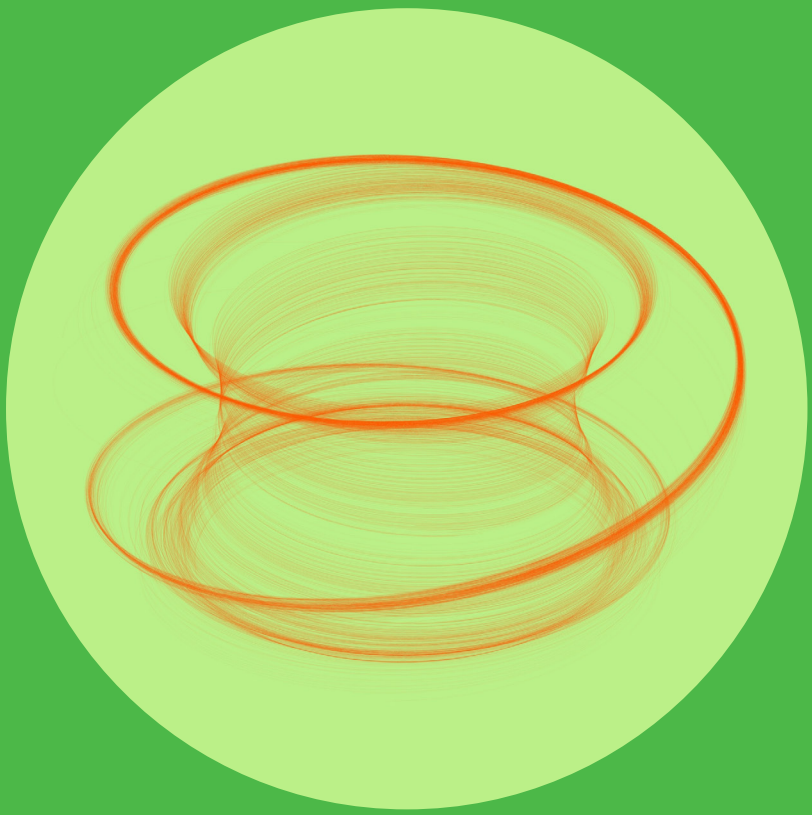

Aalto University

DOCTORAL DISSERTATIONS

Aalto University publication series
DOCTORAL DISSERTATIONS 61/2015

Modelling of global impurity transport in tokamaks in the presence of non-axisymmetric effects

Juho Miettunen

A doctoral dissertation completed for the degree of Doctor of Science (Technology) to be defended, with the permission of the Aalto University School of Science, at a public examination held at the lecture hall F239a of the school on 29 May 2015 at 12 noon.

Aalto University
School of Science
Department of Applied Physics
Fusion and Plasma Physics

Supervising professor
Associate Professor Mathias Groth

Thesis advisor
Adjunct Professor Taina Kurki-Suonio

Preliminary examiners
Associate Professor Masahiro Kobayashi, National Institute for Fusion Science, Japan
Assistant Professor Oliver Schmitz, University of Wisconsin-Madison, USA

Opponent
Professor Detlev Reiter, Forschungzentrum Jülich, Germany

Aalto University publication series
DOCTORAL DISSERTATIONS 61/2015

© Juho Miettunen

ISBN 978-952-60-6189-4 (printed)
ISBN 978-952-60-6190-0 (pdf)
ISSN-L 1799-4934
ISSN 1799-4934 (printed)
ISSN 1799-4942 (pdf)
http://urn.fi/URN:ISBN:978-952-60-6190-0

Unigrafia Oy
Helsinki 2015

Finland

441 697
Printed matter

Aalto University

Abstract

Aalto University, P.O. Box 11000, FI-00076 Aalto www.aalto.fi

Author
Juho Miettunen

Name of the doctoral dissertation
Modelling of global impurity transport in tokamaks in the presence of non-axisymmetric effects

Publisher School of Science

Unit Department of Applied Physics

Series Aalto University publication series DOCTORAL DISSERTATIONS 61/2015

Field of research Engineering Physics

Manuscript submitted 20 January 2015 **Date of the defence** 29 May 2015

Permission to publish granted (date) 2 April 2015 **Language** English

☐ **Monograph** ☒ **Article dissertation (summary + original articles)**

Abstract

Understanding and control of plasma-surf ace interaction together with the subsequent migration of eroded impurity particles form one of the key challenges for reactor-scale magnetic confinement fusion devices such as tokamaks. An aspect of impurity migration that requires further investigation is the influence of non-axisymmetric (3D) features of tokamaks.

In this work, global impurity transport is simulated in the ASDEX Upgrade and JET tokamaks with the Monte Carlo orbit-following code ASCOT. The simulations address experiments conducted on these devices, using tracer impurities injected into the plasma in a gaseous form, and via special wall tiles installed into the torus. The presented simulations are carried out in a realistic tokamak environment with an unrestricted computational domain and employing 3D descriptions of the wall geometry and the magnetic field.

According to the ASCOT predictions, accounting for the non-axisymmetric wall geometry can be crucial in interpreting the experimentally measured tracer deposition profiles. In particular, studies of ASDEX Upgrade indicate that the impurity deposition pattern on plasma-facing surfaces can exhibit substantial asymmetry in the toroidal direction due to the three-dimensional nature of the wall geometry, in contrast to previous assumptions. For 3D features of the tokamak magnetic field, the simulations predict toroidal field ripple and resonant magnetic perturbations to induce local modifications into the deposition pattern.

The presented simulation results highlight the role of plasma conditions in determining the impurity birth profile and the ratio between main chamber and divertor deposition. Besides the divertor configuration, the main mode of operation in modern tokamaks, it is shown that also the limiter configuration can lead to long-range impurity transport within the torus.

The results of this work suggest that increased attention should be directed towards the non-axisymmetric features of tokamaks for a reliable assessment of impurity migration in next-step devices.

Keywords fusion, tokamak, impurities, transport, deposition

ISBN (printed) 978-952-60-6189-4 **ISBN (pdf)** 978-952-60-6190-0

ISSN-L 1799-4934 **ISSN (printed)** 1799-4934 **ISSN (pdf)** 1799-4942

Location of publisher Helsinki **Location of printing** Helsinki **Year** 2015

Pages 124 **urn** http://urn.fi/URN:ISBN:978-952-60-6190-0

Tekijä
Juho Miettunen

Väitöskirjan nimi
Modelling of global impurity transport in tokamaks in the presence of non-axisymmetric effects

Julkaisija Perustieteiden korkeakoulu

Yksikkö Teknillisen fysiikan laitos

Sarja Aalto University publication series DOCTORAL DISSERTATIONS 61/2015

Tutkimusala Teknillinen fysiikka

Käsikirjoituksen pvm 20.01.2015 **Väitöspäivä** 29.05.2015

Julkaisuluvan myöntämispäivä 02.04.2015 **Kieli** Englanti

☐ **Monografia** ☒ **Yhdistelmäväitöskirja (yhteenveto-osa + erillisartikkelit)**

Tiivistelmä

Plasma-seinä-vuorovaikutuksen ja siitä aiheutuvan erodoituneiden epäpuhtaushiukkasten leviämisen ymmärtäminen ja hallinta muodostavat erään tärkeimmistä haasteista reaktoritason magneettisen koossapidon fuusiolaitteille kuten tokamakeille. Tokamakien ei-aksisymmetriset eli kolmiulotteiset piirteet ovat yksi epäpuhtauksien leviämisen osa-alue, joka vaatii lisätutkimuksia.

Tässä työssä simuloidaan epäpuhtauksien globaalia kulkeutumista ASDEX Upgrade- ja JET-tokamakeilla käyttäen Monte Carlo -pohjaista ASCOT-radanseurantakoodia. Simulaatiot käsittelevät näillä laitteilla tehtyjä kokeita, joissa merkkiaine-epäpuhtauksia on vapautettu plasmaan sekä injektiolla kaasumaisessa muodossa että käyttäen erityisiä torukseen asennettuja seinätiiliä. Esitellyt simulaatiot suoritetaan realistisessa tokamak-ympäristössä rajattomassa laskenta-alueessa ja hyödyntäen sekä seinägeometriaa että magneettikenttää kolmiulotteisessa muodossa.

ASCOT-simulaatioiden mukaan ei-aksisymmetrisen seinägeometrian huomioiminen voi olla hyvin tärkeää kokeellisesti mitattujen merkkiaineiden kerrostumisprofiilien oikean tulkinnan kannalta. Erityisesti ASDEX Upgradea käsittelevät tutkimukset osoittavat, että epäpuhtauksien kerrostumisessa seinäpinnoille voi ilmetä huomattavaa epäsymmetriaa toroidaalisessa suunnassa seinägeometrian kolmiulotteisten piirteiden vuoksi, mikä on vastoin aiempia oletuksia. Magneettikentän kolmiulotteisiin piirteisiin liittyen simulaatiot ennustavat toroidaalisen väreen ja ulkoisten magneettisten häiriöiden aiheuttavan lokaaleja muutoksia epäpuhtauksien kerrostumiseen.

Esitetyt simulaatiotulokset korostavat plasmaolosuhteiden merkitystä epäpuhtauksien syntyprofiilin ja diverttorikerrostumisen määrittäjänä. Modernien tokamakien pääasiallisesti käyttämän diverttorikonfiguraation lisäksi myös limitterikonfiguraation ennustetaan johtavan laaja-alaiseen epäpuhtauksien kulkeutumiseen toruksen alueella.

Työn tulosten perusteella tokamakien ei-aksisymmetrisiin piirteisiin tulisi kiinnittää enemmän huomiota luotettavien arvioiden saamiseksi epäpuhtauksien leviämisestä seuraavan sukupolven laitteissa.

Avainsanat fuusio, tokamak, epäpuhtaudet, kulkeutuminen, kerrostuminen

ISBN (painettu) 978-952-60-6189-4 **ISBN (pdf)** 978-952-60-6190-0

ISSN-L 1799-4934 **ISSN (painettu)** 1799-4934 **ISSN (pdf)** 1799-4942

Julkaisupaikka Helsinki **Painopaikka** Helsinki **Vuosi** 2015

Sivumäärä 124 **urn** http://urn.fi/URN:ISBN:978-952-60-6190-0

Preface

The research presented in this thesis has been carried out in the Fusion and Plasma Physics group at Aalto University, School of Science during 2011–2014. The work was begun under the supervision of Rainer Salomaa who was then followed by Mathias Groth. I am grateful to both of them for enabling me to dig into fusion energy, and I feel that what I have learned will always hold its value, no matter where I will be.

I would like to thank my thesis advisor Taina Kurki-Suonio for the guidance I have received over the years. In particular, my research topic has been proven to be extremely fruitful and this has allowed me to progress rather smoothly to this point.

I am indebted to the developers at Aalto University for making ASCOT the versatile simulation tool it is today. I thank Otto Asunta, Eero Hirvijoki, Tuomas Koskela, Seppo Sipilä, Antti Snicker, Simppa Äkäslompolo and all the others who have made my work so easy.

Regarding scrape-off layer physics, I owe a great deal of what I have learned to Mathias, and it is his vast scientific expertise that has kept my work solid. Furthermore, my modelling work would not have been possible without the efforts of Toni Makkonen, Markus Airila and Ville Lindholm, and I am thankful for their contributions together with everyone else that I have collaborated with.

For the experimental work and the opportunities for modelling my thanks go to Antti Hakola and Jari Likonen (VTT, Finland) together with Henric Bergsåker (KTH, Sweden) and co-workers. I appreciate the way I have been able to link my work to the reality, and naturally credit should be given also to the people at Max-Planck-Institut für Plasmaphysik and Culham Centre for Fusion Energy who have made the experiments possible.

I thank my parents for the freedom I have always had in making my own decisions, leading to the completion of this thesis. To all the people around me, I am grateful for the things that have given me so much joy outside work.

Aira, thank you for all the fun times we have had together and for the various ways you have supported this work and everything else. I hope that some day I can be as much help to you as you have been to me.

Espoo, April 22, 2015,

Juho Miettunen

This work has been carried out within the framework of the EUROfusion Consortium and has received funding from the European Union's Horizon 2020 research and innovation programme under grant agreement number 633053 and from Tekes – the Finnish Funding Agency for Innovation. The views and opinions expressed herein do not necessarily reflect those of the European Commission.

The supercomputing resources of CSC – IT Center for Science were utilized in the studies, and also the resources of HPC-FF are greatly acknowledged. This work was partially funded by the Academy of Finland project Nos. 134924 and 259675.

Contents

List of Publications

This thesis consists of an overview and of the following publications which are referred to in the text by their Roman numerals.

I J. Miettunen, T. Kurki-Suonio, T. Makkonen, M. Groth, A. Hakola, E. Hirvijoki, K. Krieger, J. Likonen, S. Äkäslompolo and the ASDEX Upgrade Team. The effect of non-axisymmetric wall geometry on ^{13}C transport in ASDEX Upgrade. *Nuclear Fusion*, **52** 032001, 2012.

II J. Miettunen, M.I. Airila, T. Makkonen, M. Groth, V. Lindholm, C. Björkas, A. Hakola, H.W. Müller and the ASDEX Upgrade Team. Dissociation of methane and nitrogen molecules and global transport of tracer impurities in an ASDEX Upgrade L-mode plasma. *Plasma Physics and Controlled Fusion*, **56** 095029, 2014.

III J. Miettunen, M.I. Airila, M. Groth, V. Lindholm, T. Makkonen, S. Äkäslompolo and the ASDEX Upgrade Team. Influence of toroidal field ripple and resonant magnetic perturbations on global ^{13}C transport in ASDEX Upgrade. Accepted for publication in *Journal of Nuclear Materials*, doi:10.1016/j.jnucmat.2014.10.095, 2014.

IV J. Miettunen, M. Groth, T. Kurki-Suonio, H. Bergsåker, J. Likonen, S. Marsen, C. Silva, S. Äkäslompolo and JET EFDA Contributors. Predictive ASCOT modelling of ^{10}Be transport in JET with the ITER-like wall. *Journal of Nuclear Materials*, **438** S612, 2013.

Author's Contribution

Publication I: "The effect of non-axisymmetric wall geometry on ^{13}C transport in ASDEX Upgrade"

The author performed the ASCOT simulations and had a leading role in the analysis of the results. The article and the figures were prepared by the author and revised according to comments from the co-authors.

Publication II: "Dissociation of methane and nitrogen molecules and global transport of tracer impurities in an ASDEX Upgrade L-mode plasma"

The author performed the ASCOT simulations and had a leading role in the analysis of the results. He also provided input data for the ERO simulations and had a major role in the analysis of the ERO results. The article and the figures were prepared by the author and revised according to comments from the co-authors.

Publication III: "Influence of toroidal field ripple and resonant magnetic perturbations on global ^{13}C transport in ASDEX Upgrade"

The author performed the ASCOT simulations and had a leading role in the analysis of the results. The article and the figures were prepared by the author and revised according to comments from the co-authors.

Publication IV: "Predictive ASCOT modelling of ^{10}Be transport in JET with the ITER-like wall"

The author performed the ASCOT simulations and had a leading role in the analysis of the results. He also created the background plasma for the limiter configuration and the 3D wall geometry used in the simulations. The article and the figures were prepared by the author and revised according to comments from the co-authors.

1. Introduction

1.1 Nuclear fusion as an energy source

Energy production has become an indispensable part of the development of all modern societies. While currently dominant fossil fuels are diminishing [1], their role is also being reconsidered due to the increasing evidence regarding the impact of greenhouse gas emissions on climate change [2]. Simultaneously, the global energy demand is substantially increasing together with the rising population and standard of living in, e.g., China, India and the Middle East, and hundreds of millions of people are expected to start using electricity by 2050 [1]. Although each of these issues poses a challenge independently, it is their combined effect that so urgently calls for a transformation in the way energy is produced.

Together with alternative ways of utilising the present resources of fossil fuels (such as shale oil), the energy challenge is being addressed with renewable energy sources (mostly solar and wind power) and fission-based nuclear power. However, as already envisaged in the 1950s, also nuclear fusion offers an attractive component to the energy mix.

Fusion power is based on *fusion reactions* where nuclei of light elements are brought together to fuse into heavier elements. When the binding energy per nucleon is increased in the process, this results in the release of energy. Current research is focused on the fusion between the heavy isotopes of hydrogen, deuterium (D, ^{2}H) and tritium (T, ^{3}H), with the reaction

$$\mathrm{D} + \mathrm{T} \rightarrow\ ^4\mathrm{He}\ (3.5\ \mathrm{MeV}) + \mathrm{n}\ (14.1\ \mathrm{MeV}), \tag{1.1}$$

where 17.6 MeV of energy is released as the kinetic energy of the resulting alpha particle and the neutron. The advantages of D-T fusion are its high reaction cross section at feasible temperatures (peak value at 40 keV) and

the availability of the reactants. Deuterium can be extracted from sea water and is thus abundant, whereas tritium can be bred from lithium with neutron bombardment produced in the D-T reaction itself.

To generate fusion reactions, the electromagnetic repulsion of the positive nuclei has to be overcome by bringing them so close to each other that the strong nuclear force can take over. In practice, this implies a high kinetic energy for the reactants which can be achieved with a high temperature of the order of 10 keV (100 million degrees). At such high temperatures, atoms become stripped of their electrons and matter turns into the state of a *plasma*.

Fusion power is pursued mainly with two fundamentally different concepts. Inertial confinement fusion aims at achieving a high plasma density using commonly powerful and carefully aligned lasers. The objective of magnetic confinement fusion, for its part, is to achieve good plasma confinement with the help of a magnetic field.

The rationale for developing fusion power becomes evident when considering its benefits. Fusion power offers vast amounts of baseload energy without direct greenhouse gas emissions and the fuel resources are abundant. The reactors are safe to operate and the potential for nuclear proliferation is low [3]. Radioactivity is limited to the consumed tritium (half-life 12.3 years) and the activation of materials surrounding the plasma due to the neutrons.

As manifested by the lack of fusion power in our everyday lives, generating net energy in potential reactors has proven to be an unforeseen challenge from both scientific and engineering perspectives. This forms the breeding ground for the most severe criticism fusion research is facing: the required effort and funding devoted to fusion has exceeded expectations, stealing focus from the development of other forms of energy [4]. Nevertheless, the progress in fusion research has been rapid (even surpassing Moore's law in computing hardware) providing encouragement. The current focal point is ITER, a next-step magnetic confinement device employing the concept of a *tokamak* which aims at producing 500 MW of fusion power, demonstrating the viability of fusion as an energy source [5].

1.2 Tokamaks

1.2.1 Prerequisites for energy production

Substantial heating power is required to generate a high-temperature plasma and to compensate for power that is lost, e.g., due to radiation. Net energy is thus produced only when fusion power exceeds the heating power and losses. Fortunately, the fusion products themselves (alpha particles in the case of D-T fusion) can provide internal heating. This enables to reach *ignition* which creates a self-sustaining state where the power from fusion reactions is sufficient to maintain the plasma temperature without any external heating [6].

The Lawson criterion states that the product of the plasma ion density and energy confinement time $n_i\tau_E$ has to exceed a certain minimum value to reach ignition [7]. As also the plasma ion temperature T_i is of relevance, a more common figure of merit is the *fusion triple product* for which the minimum required value for ignition can be estimated to be [6]

$$n_i\tau_E T_i > 5 \times 10^{21}\ \mathrm{m}^{-3}\ \mathrm{s\ keV}, \tag{1.2}$$

with the exact value depending on assumptions used. This can be achieved with, e.g., $n_i = 10^{20}$ m^{-3}, $\tau_E \approx 3.3$ s and $T_i = 15$ keV, conditions that are feasible in a tokamak. In past and current tokamaks, a value of $n_i\tau_E T_i = 1.5 \times 10^{21}$ m^{-3} s keV has been reached on the Japanese JT-60U device [8].

1.2.2 Operating principle

The primary idea in a tokamak is to achieve good confinement (maximise τ_E) for the charged plasma particles using a magnetic field. Plasma is created inside a torus-shaped vacuum chamber which is provided with a helical magnetic field consisting of toroidal and poloidal components as illustrated in Figure 1.1. A pure toroidal magnetic field, created using a set of toroidal field (TF) coils, is not sufficient to confine the plasma due to drifts that emerge on particle orbits (Section 4.3.1). An additional poloidal magnetic field is therefore imposed by inducing a plasma current inside the chamber with a transformer-like action. Consequently, tokamaks are inherently pulsed devices and their operation consists of individual plasma discharges. As the magnetic field strength is highest on the inner part of the torus, this region is often referred to as *high-field side*

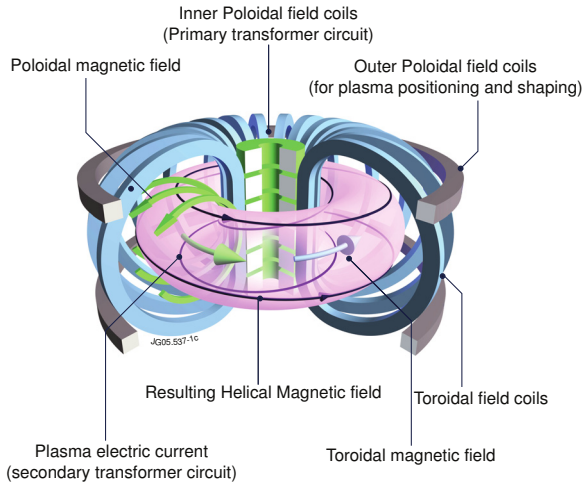

Figure 1.1. Operating principle of a tokamak showing also the poloidal and toroidal directions. *Courtesy of EUROfusion*.

(HFS) and, correspondingly, the outer part as *low-field side* (LFS).

Even the most sophisticated magnetic configurations, however, are unable to provide perfect confinement. In a tokamak, the dominant contribution to confinement degradation comes from plasma turbulence [9]. Besides increasing power losses, the imperfect confinement also results in interaction of the plasma with the material surfaces surrounding it in the vacuum chamber, *plasma-surface interaction* (PSI). This interaction leads to release of *impurities* from the wall into the plasma.

The confined *core plasma* region consists of magnetic field lines forming closed *magnetic flux surfaces*. Outside the core plasma lies the thin *scrape-off layer* (SOL) region of open magnetic flux surfaces connecting the plasma directly to the vessel wall. The first tokamak experiments employed the *limiter configuration* where the SOL plasma, bounded by the *last closed flux surface* (LCFS), directly connects to a *limiter* structure as illustrated in Figure 1.2. However, a large drawback of the limiter configuration is the penetration of impurities into the core plasma where they lead to substantial power losses due to radiation (Section 2.1). Modern tokamaks, therefore, rely on the *divertor configuration* with a magnetic field that diverts the SOL plasma towards specified *divertor targets*, separated from the core plasma (see Figure 1.2).

The divertor configuration is created by modifying the poloidal magnetic field with additional coils which results in a null of the poloidal field at the *X-point*. The X-point lies at the *separatrix* that separates the core plasma

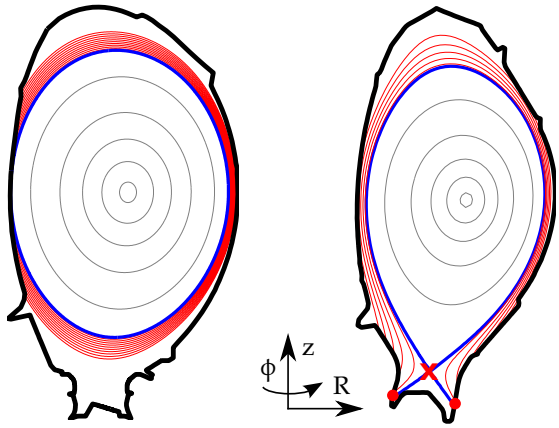

Figure 1.2. Magnetic flux surfaces in a limiter configuration in JET (left) and in a divertor configuration in ASDEX Upgrade (right). The core plasma (grey) is separated from the scrape-off layer (red) by the last closed flux surface or the separatrix (blue). Also shown are the X-point (cross) and the strike points (circles) of the divertor configuration together with the (R,ϕ,z) coordinate system.

and the SOL and connects with the inner and outer divertor targets at the *strike points*. The part of the SOL plasma closest to the separatrix, the *divertor-SOL*, is formed by magnetic field lines that connect the inner and outer divertor targets. Closer to the wall, the field lines are in contact also with the main chamber wall in the *far-SOL* and the *halo plasma*.

While current tokamaks mainly operate diverted plasmas, the limiter configuration is still present during the start-up and shutdown phases of plasma discharges, even in ITER. During these phases, plasma current is increased to its steady state value for the *flattop* phase of the discharge and then correspondingly terminated.

Most of plasma heating is achieved with the injection of energetic neutral particles into the plasma (neutral beam injection, NBI) and using radiofrequency waves to transfer energy mainly to ions (ion cyclotron resonant heating, ICRH) or electrons (electron cyclotron resonant heating, ECRH).

High-performance tokamak operation is based on the *high-confinement mode* (H-mode). Experimentally, it has been observed that as the heating power exceeds a certain threshold value, the confinement is abruptly improved as the plasma experiences a transition from the *low-confinement mode* (L-mode) to the H-mode [10]. H-mode operation, however, is compromised by *edge localised modes* (ELMs), i.e., repetitive and fast expul-

sions of particles and energy from the plasma [11]. As ELMs carry large amounts of energy (even 30 MJ for a single ELM in ITER [12]), they pose a threat to the lifetime and integrity of the plasma-facing components (PFCs).

Tokamaks are often described using an (R,ϕ,z) coordinate system where R is the horizontal distance from the centre of the torus, z the corresponding vertical distance and ϕ the toroidal angle as visualised in Figure 1.2. The size of the device is characterised by the distances from the centre of the plasma to the centre of the torus (major radius R_0) and to the edge of the plasma (minor radius a).

1.2.3 Non-axisymmetric features in tokamaks

In an ideal sense, a tokamak can be approximated as an axisymmetric system. Its magnetic field does not appear to exhibit substantial deviations from toroidal symmetry and a smooth, toroidally symmetric surface could be expected to surround the plasma. This forms also the basis for most of the theoretical analysis and modelling of tokamak plasmas, greatly simplifying these studies by allowing the spatial domain to be reduced to the two-dimensional (R,z) plane.

In reality, the toroidal magnetic field possesses toroidal non-uniformity. As the toroidal field is created using a finite number of coils (recall Figure 1.1), its strength is highest near a coil and lowest between two adjacent coils as can be concluded from Figure 1.3.

Toroidal variation of the magnetic field strength, *toroidal field ripple*, is therefore always present in tokamaks with its magnitude depending on the device (decreasing with the number of TF coils), and also position inside the torus (highest on the LFS). In the ASDEX Upgrade tokamak with 16 TF coils, ripple magnitude reaches a value of the order of 1 % of the toroidal magnetic field near the outer wall.

TF ripple has been deemed significant regarding, e.g., the confinement of the highly energetic fusion alphas [13, 14]. Considering ITER, the magnetic field is also locally perturbed due to components such as test blanket modules (TBMs) that will be used to investigate tritium breeding [15].

A more prominent display of additional non-axisymmetric features in a tokamak magnetic field is due to *resonant magnetic perturbations* (RMPs) that represent a promising candidate for ELM mitigation [12]. RMPs are generated using a set of special in-vessel coils, distributed toroidally around the entire torus and poloidally within the low-field side. The ELMs

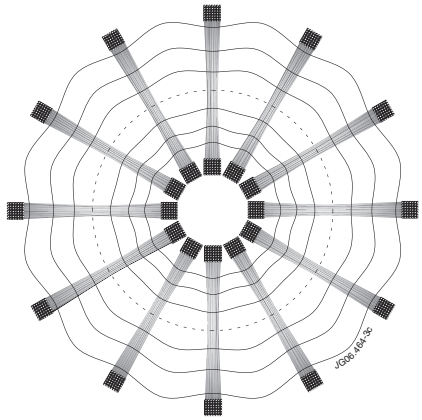

Figure 1.3. Illustration of toroidal field ripple as viewed from the above. Due to the finite number of toroidal field coils (grey), the magnetic field strength oscillates toroidally and the field protrudes outwards (towards the wall) in regions between adjacent coils. *Courtesy of EFDA-JET.*

are mitigated as a result of small magnetic perturbations that reduce confinement at the edge of the core plasma. Following encouraging results from, e.g., the DIII-D [16] and ASDEX Upgrade [17] tokamaks, RMP coils will likely be utilised also in ITER [18]. The complication brought by RMPs, however, is that they render the magnetic field topology truly three-dimensional. Regarding the SOL, this has already been shown to result in, e.g., a perturbation of the separatrix and subsequent striated particle flux patterns on the divertor [19–21].

Furthermore, a fully axisymmetric wall geometry for a tokamak is typically not achieved in practice. As shown in Figure 1.4, protruding wall structures appear in particular at the low-field side of the vessel consisting of, e.g., limiters and antennas for radiofrequency heating.

Tokamaks, therefore, exhibit non-axisymmetric features both in their magnetic field and wall geometry. When progressing towards quantitative studies of next-step devices such as ITER, 3D phenomena are rising to a more prominent role in fusion research. Owing to advances in the capabilities of computers and numerical simulation codes, the effects of these non-axisymmetric features in tokamaks can be investigated with modelling.

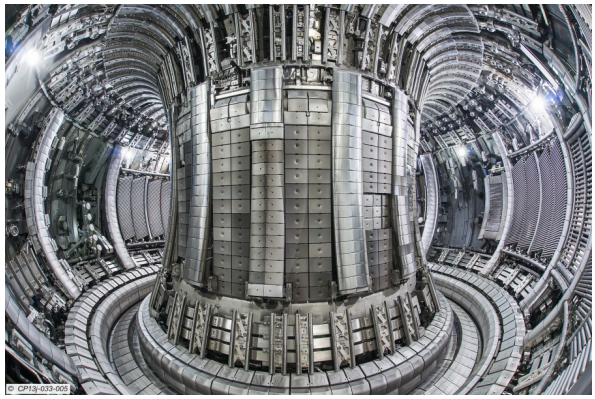

Figure 1.4. A view inside the JET tokamak after the 2012–2013 experimental campaign. The vertical protruding structures at the central column are inner-wall guard limiters. Additional limiters and antennas for radiofrequency heating can be seen on the outer wall causing toroidal asymmetry. *Courtesy of EUROfusion*.

1.3 Scope of the thesis

This thesis focuses on numerical simulations of global impurity transport in tokamaks taking into account the non-axisymmetric nature of both the wall geometry and the magnetic field. The simulations model experimental studies of the migration of tracer impurities that have been conducted on two major tokamaks currently in operation, ASDEX Upgrade (AUG) and JET. Transport of the impurities is simulated with the 3D orbit-following Monte Carlo code ASCOT that allows a fully unrestricted computational domain inside the tokamak. Besides aiding the preparation and interpretation of the experiments, one of the central objectives of this work is to provide predictions of the influence of the non-axisymmetric features in tokamaks on global impurity transport. In addition to the 3D features, the simulations also address the impact of the impurity birth distribution on their transport in the plasma and transport in a limiter configuration.

The thesis is organised in the following manner. In Chapter 2, the influences of impurities on tokamak operation are described as well as the basic processes contributing to global migration of impurities in tokamaks. Chapter 3 presents two experimental techniques that have been used for studying impurity migration: tracer injection and marker tiles. Conducted experiments with these techniques on ASDEX Upgrade (^{13}C and ^{15}N tracer injection) and JET (^{10}Be marker tile) are described. Chapter 4 motivates the need for numerical simulations of the experiments

and presents the simulation codes that have been employed in this work together with their theoretical basis. The main results of Publications I–IV that have been obtained during the course of this work are outlined in Chapter 5. Finally, Chapter 6 concludes the work, and the avenues that are open for further research are described.

2. Impurity migration in tokamaks

2.1 Impurities in tokamak plasmas

In the dawn of magnetic confinement fusion research in the 1950s, the main attention was drawn towards the (hydrogenic) core plasma. After all, the core occupies the clear majority of the plasma volume and, as stated in Equation 1.2, high plasma temperature, density and confinement time in the core are needed for producing fusion reactions. Nevertheless, it soon became evident that plasma-surface interaction and the subsequent release of impurities can have profound influence on tokamak operation as radiation caused by the impurities was observed to be among the dominant energy loss mechanisms of the plasma. With increasing knowledge about PSI and impurities, Soviet scientists were able to reach an electron temperature of 1 keV in 1968 in the T-3 tokamak [22, 23]. The result became a milestone in fusion research, encouraging scientists around the world to focus their efforts on the tokamak concept. Still today, plasma-surface interaction remains one of the largest challenges for reactor-scale fusion devices.

Impurities have rather diverse effects on tokamak operation. These effects are closely linked with the choice of wall materials since plasma-facing surfaces act as impurity sources. In addition, helium is an intrinsic impurity species created in fusion reactions, most notably D-T fusion. Furthermore, impurities can also be deliberately seeded into the SOL plasma for power exhaust purposes.

Firstly, impurities cause *radiation losses*, mainly in the form of line radiation and bremsstrahlung, which unfavourably lower the central temperature if present in the core plasma. At relevant core plasma temperatures of several keVs, heavy impurities (high Z number) result in orders

of magnitude higher radiation losses compared to light impurities and, in this respect, low-Z wall materials such as beryllium (Be, $Z = 4$) and carbon (C, $Z = 6$) are desirable [24]. In contrast, it should be noticed that in the SOL plasma radiation is beneficial as it helps to distribute the power exhausted from the core plasma over large surface areas.

A further disadvantage of impurities in the core plasma is *fuel dilution*. To prevent the onset of plasma instabilities, plasma pressure (and hence its density) has to remain sufficiently low with respect to the magnetic pressure [6]. As impurities contribute to electron density in the core plasma, this reduces the achievable density of the hydrogenic fuel particles.

However, also the *erosion* of the plasma-facing components under incoming plasma flux has to remain sufficiently low so that a long lifetime for the components can be achieved. In general, high-Z materials are more resilient to erosion, and materials such as tungsten (W, $Z = 74$) present a favourable solution for regions of high heat flux.

Considering only radiation losses and PFC lifetime, carbon is a suitable candidate for a tokamak wall material as it combines the low-Z property with excellent thermomechanical capabilities [25]. Despite these advantages, the mechanical properties degrade under neutron irradiation [26]. An additional drawback regarding operation with a carbon wall is the formation of hydrogen-rich carbon layers on the PFCs. In a reactor-scale device using a D-T fuel, these layers also contain tritium which leads to *tritium retention*. As tritium is radioactive, its inventory in, e.g., ITER is strictly controlled by nuclear licensing [27]. Furthermore, global tritium resources are limited and, therefore, as much tritium as possible should be recovered from deposits and re-used as fuel. The issue of tritium retention has recently resulted in the abandonment of carbon as the wall material in future reactor-scale devices.

In ITER, beryllium will be used in the main chamber region of the torus, whereas the divertor will be of tungsten[1]. This materials configuration provides resilience to high heat and particle fluxes at the divertor and simultaneously allows high plasma performance even in the presence of impurity radiation due to main chamber erosion. In JET, the same materials have been subject to extensive studies in the *ITER-like wall* project [30].

[1]The original design employed carbon fibre composite in the strike-point regions of the divertor during the initial non-active (non-DT) phase of operation [28]. Later investigation, however, proved the full-tungsten alternative feasible already for the initial phase [29].

2.2 Global migration of impurities

The migration of impurities, consisting of a cyclic set of erosion, transport and deposition processes, strongly influences how the effects described in Section 2.1 are manifested in a tokamak. Considering power losses in the core plasma, the radiation resulting from impurities is linked to the strength of the penetration of the impurities from the wall and SOL towards the core. Furthermore, the *net* erosion actually observed on PFCs is lower than the nominal gross erosion as eroded particles can be deposited in the proximity of the erosion location. Regions of highest tritium retention, for its part, are correlated with net deposition regions determined by the impurity migration pattern.

Additionally, impurity migration also creates an entirely new issue in the form of *material mixing*. In the ITER-like scenario, beryllium eroded from the main chamber can be transported and deposited at the tungsten divertor creating W-Be alloys. This can be detrimental as experiments, e.g., on the linear plasma device PISCES-B have indicated that the melting temperature of tungsten is substantially lowered by the presence of beryllium [31].

As a consequence, the assessment of the influence of plasma-surface interaction and impurities on tokamak operation requires understanding how impurity migration occurs in a plasma. Firstly, the erosion of plasma-facing surfaces that leads to the generation of impurities occurs mainly through physical and chemical sputtering [24]. In physical sputtering, typically neutral atoms from the surface are ejected due to momentum transferred by the impinging plasma particles. The average number of sputtered particles per incident particle, the sputtering yield, depends strongly on both the substrate material and the impinging particle species together with its impact energy and angle. Chemical sputtering, for its part, takes place when the impinging particle reacts chemically with the surface lattice (e.g., H/D/T with C) resulting in the formation of a molecule. Unlike physical sputtering, chemical sputtering yield is mainly dependent on the substrate temperature, and weakly on the incoming ion flux [32].

The generated impurities subsequently experience *transport* in the plasma. In long-range transport, ionised impurities can travel large distances in the torus and even penetrate into the core plasma. Short-range transport, in contrast, retains the impurities in the proximity of their birth lo-

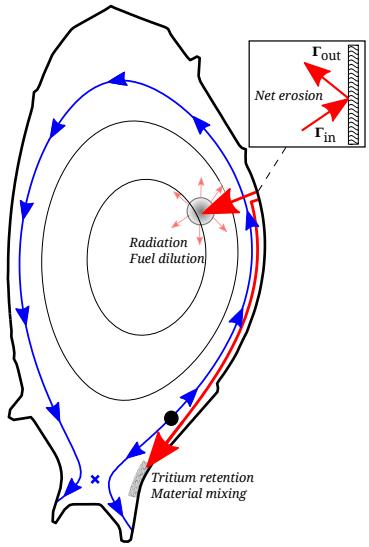

Figure 2.1. The impact of impurity migration on tokamak operation (red arrows): radiation power losses and fuel dilution in the core plasma, tritium retention in surface layers, material mixing due to long-range transport, and net erosion as determined by the competition between the eroded (Γ_{out}) and deposited (Γ_{in}) particle fluxes. The blue arrows illustrate the typically assumed plasma flow pattern in the SOL (lower single-null configuration with ion $\mathbf{B}\times\nabla B$ drift towards the lower divertor) showing the stagnation point in black [33, 34].

cation. In the extreme case of prompt re-deposition, the ionisation mean free path of a sputtered neutral is so short that the particle is immediately deposited on the eroded surface.

Impurity transport in the SOL is governed by both neoclassical and turbulent transport as will be discussed in Section 4.3. In the direction parallel to the magnetic field, *plasma flow*, the collective motion of the plasma, plays a large role for long-range transport. The flow magnitude is commonly expressed in terms of the ratio between the flow velocity and plasma sound speed, the Mach number

$$M = \frac{v_{\text{flow}}}{c_{\text{s}}} = \frac{v_{\text{flow}}}{(k_B(T_e + T_i)/m_i)^{1/2}}, \tag{2.1}$$

where k_B is the Boltzmann constant, T_e and T_i the electron and ion temperatures, respectively, and m_i the ion mass. Experimental multi-machine studies in lower single-null magnetic configurations have indicated the presence of strong (around Mach 0.5) plasma flows in the main chamber which accelerate towards a Mach 1.0 velocity at the divertor [33, 34]. As visualised in Figure 2.1, a stagnation point is concluded to lie somewhere between the outer midplane and the X-point, directing most of the flow-driven transport towards the inner divertor.

Transport in the open magnetic field lines of the SOL inevitably leads to interaction with the wall. At the wall surface, the incoming impurity particle can experience reflection, followed by continued transport in the plasma. If no reflection takes place, *deposition* of the particle on the surface occurs.

The deposited particle can then be re-eroded, transported in the plasma and re-deposited. This cyclic behaviour of erosion, transport and deposition constitutes *impurity migration*[2] and can consequently transfer material over large distances inside the torus.

As impurity migration is in such a pivotal role in reactor-scale fusion devices, it has been a subject of long-standing studies typically combining both experiments and numerical simulations [35, 36]. While a complete picture of impurity migration is yet to be formed, one of the key observations in numerous studies (in particular tracer injection experiments, Section 3.1) has been the general tendency of the migration to be directed towards the inner divertor, thus making it a region of net impurity deposition [28]. This has been presumed to be due to flow-driven transport in the SOL. The outer divertor has been commonly attributed as a net erosion region [28].

What still remains to be resolved is how the observed impurity migration in, e.g., L-mode plasmas of current tokamaks can be extrapolated to the high-density H-mode conditions in ITER with a Be-W materials configuration. Another aspect of impurity migration that still requires further investigation is the influence of the non-axisymmetric features of the tokamak. This forms one of the central motivations for the simulations presented in this thesis.

[2]Some authors use the word *migration* with a slightly different meaning referring more to transport instead of a set of processes described above.

3. Experimental methods for studying impurity migration

Studies of impurity migration heavily rely on experiments conducted on current tokamaks. In this Chapter, two experimental methods are presented: the injection of tracer isotopes into the plasma and the use of special marker tiles inside the torus. These methods are introduced together with specific experiments that are in the focus of this work: ^{13}C and ^{15}N injection experiments carried out on ASDEX Upgrade (Publications I–III), and a ^{10}Be marker tile experiment on JET (Publication IV).

ASDEX Upgrade is a medium-size tokamak ($R_0 = 1.65$ m) operated by Max-Planck-Institut für Plasmaphysik in Garching, Germany. In the past, the tokamak employed carbon as the plasma-facing material in the entire torus. However, after the step-wise transition during 1999–2007 [37], AUG is now a full-tungsten device.

JET (Joint European Torus), located in Abingdon, the UK, is currently the largest tokamak ($R_0 = 2.96$ m) in operation. As ASDEX Upgrade, also JET has a long history of using carbon as the plasma-facing material. In 2011, a major transformation in one single installation was completed, resulting in a beryllium main chamber and a tungsten divertor [30]. This materials configuration, the ITER-like wall, has offered a unique opportunity to gain experience of the plasma-facing materials that will be used in ITER.

3.1 Tracer injection

3.1.1 Introduction

In general, the use of tracers in scientific research has had widespread applications. In medicine, tracer isotopes such as technetium-99m are commonly used to, e.g., diagnose blood flow in different organs [38]. Per-

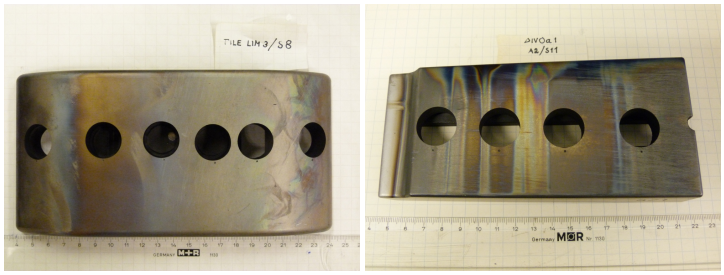

Figure 3.1. Examples of analysed wall tiles after a ^{13}C injection experiment on AUG in 2011: a limiter tile from toroidal sector 8 next to the injection port (left) and a tile from the top of the vessel (right). Distinctive signs of ^{13}C deposition can be seen in particular on the left part of the limiter tile and the top part of the second tile. Samples for surface analyses have been taken from the locations of the holes. *Courtesy of A. Hakola, VTT Technical Research Centre of Finland.*

haps the most concrete example of the use of tracers is displayed in the works of the oceanographer Curtis Ebbesmeyer. In his studies, thousands of ordinary objects including rubber ducks (acting as tracers) were washed into the Pacific Ocean to monitor ocean currents [39].

In fusion research, tracer isotopes were introduced as a method for studying impurity migration in the limiter tokamak TEXTOR [40]. The main purpose is to inject a known amount of a tracer isotope, such as ^{13}C, into a plasma with well-defined discharge conditions, typically during several consecutive and identical plasma discharges. After the experiment, a preselected set of wall tiles (see Figure 3.1) from the tokamak is removed for post mortem analysis. Surface analysis techniques, such as secondary ion mass spectrometry (SIMS) [41], can then be used to determine the tracer surface density (e.g., at/cm^2) on samples from the tiles. Collecting this data into, e.g., a poloidal deposition profile results in a representation of the preferential deposition locations of the tracer.

The chosen tracer has to fulfil a few important requirements. Firstly, the migration of the tracer has to sufficiently well correspond to the migration of the impurities of interest. For example, in the case of ^{13}C it can be expected that its migration does not substantially deviate from the migration of the standard isotope ^{12}C. In addition, the tracer has to be distinguishable from other elements present in the tokamak and the atmosphere. Carbon-13 meets this condition as it can be distinguished from ^{12}C (and other elements) by its mass. Moreover, the natural abundance of ^{13}C is only 1.1 % [42]. Finally, the tracer should not noticeably perturb the plasma conditions. In practice, this implies that injection rate of the tracer has to be kept sufficiently low.

Tracer injection experiments have become a standard method for studying impurity migration, and experiments using ^{13}C have been carried on numerous tokamaks including JET [43, 44], ASDEX Upgrade [45, 46], DIII-D [47, 48], JT60-U [49] and TEXTOR [50, 51]. For an extensive list of references and a summary of the main results, see [36]. The carbon tracer has been introduced into the torus in a gaseous form, most commonly $^{13}CH_4$ (methane) although also $^{13}CD_4$ and $^{13}C_2H_4$ (ethylene) have been used. Originally, these particular molecules were highly interesting as most of the tokamaks employed carbon as the plasma-facing material and, thus, they served as a proxy to study chemically sputtered carbon. Other used tracer gases have included SiD_4 (silane) [40], WF_6 (tungsten hexafluoride) [52] and, more recently, also nitrogen gas in the form of $^{15}N_2$ [53].

In these experiments, the injection has been performed either from a single injection valve or from multiple valves distributed in a toroidally symmetric manner. Also the injection location has been varied including the top of the vessel, the outer midplane and the outer divertor. Depending on their objective, the experiments can be classified as *local* or *global*. Local injection experiments typically address tracer deposition patterns in a certain restricted region, for example one or two wall tiles around the injection location. Combined with numerical simulations, these local studies have elucidated, e.g., carbon migration in the divertor region of ASDEX Upgrade [54, 55]. In contrast, global experiments investigate impurity migration in the entire tokamak, commonly from a main chamber source towards the divertor region.

The advantage of tracer injection experiments is that they allow the study of impurity migration during specified discharge conditions. Various parameters such as plasma density, heating power and magnetic field can be tailored for the purposes of the experiment.

However, the experimental method has also weaknesses. As the removal of multiple wall tiles from the torus can be typically done only after an experimental campaign has been finished, the experiments can be performed usually at most once a year. Furthermore, the surface analysis of the tiles is rather laborious, and practical reasons prevent the analysis of all tiles of a tokamak. The experimental results therefore represent only a sample of the total tracer deposition on the PFCs. Finally, the use of a molecular source does not perfectly mimic erosion occurring during normal operation due to physical sputtering. As presented in Publication

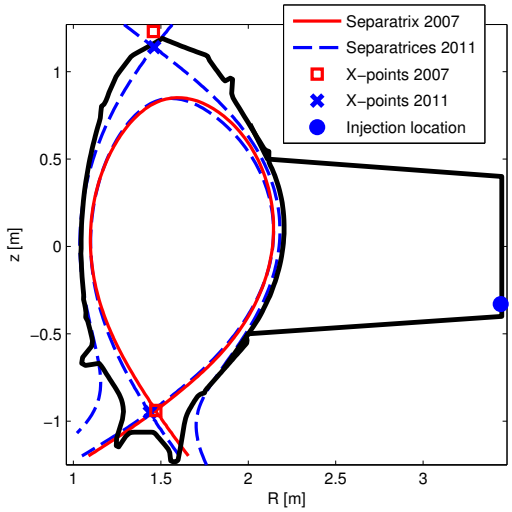

Figure 3.2. A poloidal cross section of ASDEX Upgrade showing the magnetic configurations of the 2007 (discharge #22575) and 2011 (#27385) tracer injection experiments. The lower X-points lie almost on top of each other.

II, the dissociation location of the injected molecules can deviate from the ionisation location of physically sputtered atoms which affects their migration. Despite these drawbacks, superior methods are still to find widespread application, and tracer injection remains perhaps the most useful tool for investigating impurity migration in a detailed manner.

3.1.2 Experiments on ASDEX Upgrade in 2007 and 2011

A rather extensive range of tracer injection experiments has been conducted on ASDEX Upgrade [56]. After the end of the carbon-dominated era, the first tracer injection experiment in the full-tungsten environment was performed in 2007 with ^{13}C [46]. In this experiment, $^{13}CH_4$ was injected into the torus from a single valve located poloidally at the back of an outer midplane port and toroidally in sector 9 (of 16) of AUG as shown in Figure 3.2. The injection was performed during the flattop phases of 13 consecutive, identical L-mode discharges with parameters presented in Table 3.1.

After the experiment, a set of wall tiles was removed for surface analyses, including a complete poloidal set of divertor tiles, three tiles from the inner-wall heat shield, a single tile from the top of the vessel, and two tiles from the outer wall region. Toroidally, these tiles were located in sector 11 (approximately 45° away from the injection location) except for the limiter

Table 3.1. Plasma discharge parameters for the tracer injection experiments on ASDEX Upgrade. Here, $\overline{n_e}$ is the line-averaged electron density and P_{aux} the auxiliary heating power. Both cases had a toroidal magnetic field of $B_t = -2.5$ T (ion $\mathbf{B} \times \nabla B$ drift towards the lower divertor) and a plasma current of $I_p = 0.8$ MA.

Year	Tracer	Fuel	Discharges	$\overline{n_e}$ [10^{19} m^{-3}]	P_{aux} [MW]
2007	^{13}C	D	#22573–#22585	3.3	3.4
2011	^{13}C, ^{15}N	H	#27382–#27392	5.8	2.8

Table 3.2. Estimated total ^{13}C deposition (assuming toroidal symmetry) in the 2007 and 2011 tracer injection experiments on AUG, normalised both to the amount of injected atoms and to the total estimated deposition. Here, *HS* denotes the inner-wall heat shield, *Top* the top of the vessel, *OW* the outer wall and *ID* and *OD* the inner and the outer divertors, respectively. As the estimates are based on the surface analyses of only certain PFCs, the exact numbers are subject to considerable uncertainty.

	HS	Top	OW	ID	OD
Deposition (% of injected), 2007	0.6	1	0.3	0.9	0.2
Deposition (% of total deposition), 2007	19	32	11	29	6
Deposition (% of injected), 2011	15	4	14	2	1
Deposition (% of total deposition), 2011	43	12	39	5	2

tile that originated from sector 8.

The analysed tiles showed that the deposition was strong in particular on the inner divertor (see Table 3.2), in agreement with previous tracer injection experiments. Although deposition was strong also at the top of the vessel, the total deposition in this region is difficult to estimate reliably as only a single wall tile was analysed.

When assuming toroidally symmetric deposition and integrating toroidally, the experimental results indicated that the total ^{13}C deposition was less than 10 % of the amount of injected ^{13}C. Although several explanations for the result were proposed, such as part of the methane being pumped from the torus by cryopumps, it also generated interest for investigating the possible toroidal asymmetry in the ^{13}C deposition pattern. A detailed description of the experiment and the obtained deposition profiles is presented in [46].

In 2011, a second set of tracer injection studies was conducted [56, 57]. Although the experimental scenario was largely similar as in 2007 regarding, e.g., the injection location, the plasma density was now higher (approximately 57 % of the Greenwald density) and the plasma gas was switched to hydrogen. These choices aimed at replicating the conditions

of a previous tracer injection experiment carried out in 2005 on AUG. In addition, besides ^{13}C also ^{15}N was simultaneously injected into the torus (as $^{15}N_2$) during 11 plasma discharges (see Table 3.1). Although not a wall material, nitrogen migration and its retention on PFCs have become a target of interest as nitrogen is commonly used as a seeding gas for power exhaust studies in current tokamaks [58].

When comparing the magnetic configurations of the two performed experiments (see Figure 3.2), it can be seen that in 2011 also a secondary X-point was inside the plasma and, thus, there is some resemblance to a double null configuration. As this feature can influence the transport and deposition of the tracers, it should be taken into account when comparing the experimental results for the 2007 and 2011 experiments.

As after the previous experiment, a pre-selected set of divertor and main chamber wall tiles was removed for post mortem analyses during the shutdown that followed the experiment. Significant attention in the analyses was directed towards the main chamber region[1]. Besides the divertor tiles, five additional tiles were removed from the inner wall, eight tiles from the top of the vessel and eleven tiles in total from two ICRH antennas and two outer wall limiters. Toroidally, the divertor and inner-wall tiles as well as tiles from the top of the vessel were from sectors 11 and 12, whereas limiter and ICRH tiles were chosen to address toroidal asymmetry. These included tiles from sectors 2, 8, 10 and 14, thus covering the entire torus toroidally.

In contrast to 2007, the experimental results indicated substantially increased ^{13}C deposition in the main chamber as shown in Table 3.2 [57]. Particularly high ^{13}C surface densities were found at the inner wall heat shield (10–1000 times higher than in 2007 despite no changes in the distance between the inner wall and the primary separatrix) and the outer wall. When comparing the surface densities on limiter and ICRH antenna tiles from different toroidal locations, orders of magnitude differences were observed. This was a clear demonstration that the ^{13}C deposition was not toroidally symmetric, at least not along the outer wall.

Similarly, for ^{15}N the largest tracer inventories were found from the main chamber [53]. Toroidal asymmetry was observed at the outer wall but, nevertheless, the toroidal variation of ^{15}N surface density was remarkably weaker than for ^{13}C. This result is connected with the most

[1]The choice of wall tiles removed for surface analyses was partially guided by the simulation results of Publication I as will be discussed in Section 5.1.

prominent difference between the ^{13}C and ^{15}N surface densities: whereas ^{13}C exhibited orders of magnitude differences (10^{14}–10^{19} at/cm^2), the ^{15}N surface density remained rather uniform at approximately 10^{16} at/cm^2 around the entire torus. This and the large differences between the 2007 and 2011 results for ^{13}C provided additional motivation for extensive modelling of the performed experiment. The experiment and its results for ^{13}C are presented in detail in [56, 57] and for ^{15}N in [53, 59].

The SOL plasma conditions (Section 4.1) of these 2007 and 2011 L-mode plasmas can be classified as conduction-limited or partially detached and, therefore, do not directly correspond to the detached conditions of H-mode plasmas in ITER [60]. However, understanding impurity migration in a well-defined scenario such as in the experiments allows to identify the governing physical mechanisms. This facilitates creating extrapolations to the conditions expected in ITER.

3.2 Marker tiles

3.2.1 Introduction

Besides injection as a gas, tracer impurities can be introduced into the torus also via plasma-facing components. When a traceable impurity species is present on a plasma-facing surface, it will be released into the plasma due to erosion. To study the deposition of the tracer, similar post mortem surface analyses can be performed for wall tiles removed from the tokamak as in the case of tracer injection experiments.

As the tungsten coverage of ASDEX Upgrade was being gradually increased, it became possible to investigate tungsten migration following this principle. Since carbon was still used in the rest of the PFCs, tungsten-coated tiles installed to the inner-wall heat shield effectively served as marker tiles. Post-campaign analysis of deposited tungsten on wall tiles from the divertor and the heat shield thus conveyed information about the migration pathways of eroded tungsten [61, 62]. This example also demonstrates that tracer impurities do not necessarily have to be isotopically labelled such as ^{13}C.

In addition to providing a specified source for tracers, another application of marker tiles is their use in erosion and deposition studies. Analysis of the marker tiles (containing, e.g., stripes of different elements of inter-

est) before and after their exposure to the plasma allows to quantify the erosion rate of the used material. This same approach is followed also in marker probes that can be exposed to the plasma during specified discharge conditions.

The advantage of marker tiles in impurity migration studies is that they provide a realistic impurity source. Unlike with the injection of gases, the release of impurities as a result of erosion corresponds directly to the way impurities are generated during normal tokamak operation. Additionally, marker tiles can be placed in principle anywhere in the torus. This is in contrast to tracer injection experiments where the impurities can be introduced into the plasma typically only from specific locations of the injection valves.

On the other hand, a clear drawback is that (in large tokamaks) marker tiles cannot be used only during a short experiment with specified plasma conditions. Instead, after the tiles have been installed, they typically remain inside the torus for an entire experimental campaign. As experimental campaigns can consist of hundreds of discharges resulting in hours of plasma exposure, the tiles are exposed to a wide range of plasma conditions that vary in density, heating power and confinement regime (L-mode or H-mode). Therefore, although the impurity source is specified and the resulting deposition around the torus can be investigated, the interpretation of the experimental results is challenging. The observed tracer deposition cannot be attributed to result from certain well-characterised plasmas and it is typically additionally influenced by, e.g., ELMs and plasma disruptions.

Furthermore, experiments using marker tiles can be even more laborious than tracer injection experiments. Besides the surface analysis of removed wall tiles, additional work is typically involved in processing of the tiles so that they can serve as markers, and in their installation into the torus.

The campaign-integrated nature of the marker tile experiments, however, can also be seen as an advantage. As the tracer deposition is a result of hours of plasma exposure, it gives information about the long-term migration of impurities, which is of practical consequence for reactor-scale tokamaks.

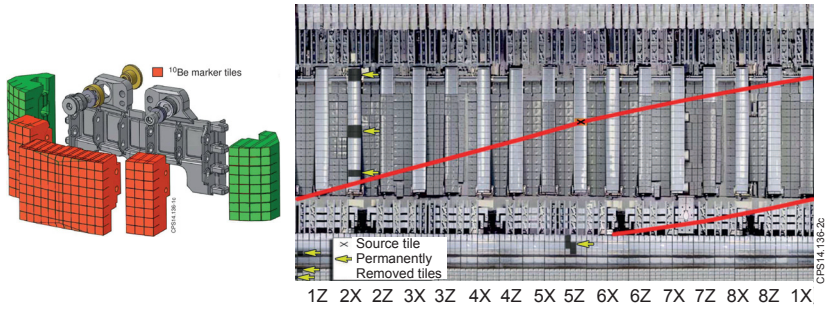

Figure 3.3. The IWGL tile assembly of the ^{10}Be marker tile experiment (left) and the position of the marker (right) on the inner-wall of JET (recall Figure 1.4). In red is shown a magnetic field line in a divertor configuration, connecting the marker to the inner divertor. The labels 1X–8Z identify the different IWGLs. *Courtesy of EFDA-JET.*

3.2.2 Experiment on JET with the ITER-like wall

To investigate beryllium migration, a marker tile experiment using ^{10}Be was initiated on JET in the ITER-like wall configuration [63]. In this experiment, three adjacent central pieces of a wall tile assembly from one of the inner-wall guard limiters (IWGLs) were enriched with ^{10}Be and installed into the torus for plasma exposure during the entire 2011–2012 experimental campaign. The tile assembly was located poloidally near the centre of the IWGL and toroidally in octant 5 (of 8) of JET as shown in Figure 3.3.

As a pioneering effort, the experiment presented the use of an isotopically labelled marker tile for the first time in impurity migration studies [63]. While ^{10}Be has not been widely used in fusion research, the isotope serves as a common tracer in geophysics and, consequently, surface analysis methods for studying its deposition are readily available [64].

During the preparation of the experiment, the IWGL tile pieces had been irradiated using the JEEP-II research (fission) reactor in Lilleström, Norway, to an isotope[2] ratio ^{10}Be/^{9}Be = 1.73×10^{-9}. The experiment provided an opportunity for a controlled study of long-term beryllium migration in general in an ITER-like environment and, furthermore, for investigating the possible material mixing that can occur in a Be-W materials configuration.

The interpretation of the experimental results of ^{10}Be deposition is challenging. Firstly, the campaign-integrated nature of the experiment im-

[2]In practice natural beryllium consists of 100 % of ^{9}Be and is hence monoisotopic [65].

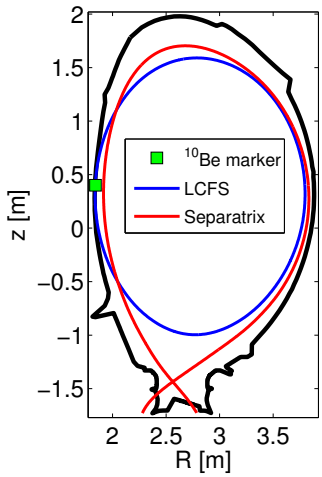

Figure 3.4. A poloidal cross section of JET showing the location of the ^{10}Be marker. The LCFS of a limiter discharge with JET pulse number (JPN) 80836 and the separatrix of a diverted discharge JPN 80295 illustrate different magnetic configurations.

plies that a large variety of different discharges have influenced the migration of the marker. Secondly, the location of the marker at the inner wall can expose it to substantial particle fluxes if the magnetic configuration is inner-wall limited (a limiter plasma with the contact point at the inner wall) as can be understood from Figure 3.4. The inner-wall limited configuration is rather common in JET during the discharge start-up and shutdown phases. From spectroscopic data it was estimated that around 90 % of the marker tile erosion during the experimental campaign had occured during limiter phases [63] and, thus, the limiter configuration is in a very central role for ^{10}Be migration.

First experimental results of ^{10}Be deposition on the IWGL tiles (limiters 2X and 5Z) were obtained using accelerator mass spectrometry (AMS) [66]. These results showed a rather non-uniform ^{10}Be deposition pattern indicating that the eroded ^{10}Be had experienced large-scale migration both poloidally and toroidally [63]. In addition, the total ^{10}Be deposition on the IWGL tiles was estimated to be only 3 % of the the amount of eroded ^{10}Be from the marker tiles. This suggests that the dominant deposition lies outside the sampled regions or even outside the entire inner wall.

These results, however, give only a preliminary view of ^{10}Be deposition as the sampled regions were limited. Further AMS studies will address deposition also in the divertor region. Besides the surface analysis, modelling will play a key role in improving the understanding of ^{10}Be migration during the experiment.

4. Modelling of impurity transport in the scrape-off layer

Although controlled experimental studies of impurity migration can be performed using the methods described in Section 3, the information obtained from these experiments is rather limited. As the source of impurities is specified and their deposition has been studied with surface analysis techniques, the principal experimental result can be expressed as “the impurities migrate from their source to their deposition location”. Even in this statement the deposition location is subject to considerable uncertainty as surface analysis cannot be performed for all of the PFCs.

The experiments, therefore, usually have a restricted capability for elucidating which physical processes actually cause the observed migration. As a result, numerical simulations of the experiments are valuable in improving the understanding of the results.

Modelling of impurity migration experiments can serve at least two important purposes, both of which are considered in this thesis. Firstly, *interpretative* simulations aim to provide reproductions of the experimental scenario after the experiment has already been completed. By varying the input parameters of the simulation model, it can be possible to match the experimentally observed tracer deposition which allows to identify governing physical mechanisms (if they are included in the model). Secondly, *predictive* simulations aid the preparation of experiments before their execution. In the case of tracer injection or marker tile experiments, they can be used to investigate which regions of the tokamak would be interesting for surface analysis. In a broader sense, the predictive capability of simulation codes is also in a prominent role when designing new fusion devices such as ITER.

Simulations of impurity migration, especially global migration, require extensive effort. In practice, none of the currently available simulation codes by itself is able to simulate the entire migration chain of the impu-

rities in the entire tokamak, at least not without considerable simplifications. In this thesis, the emphasis is on simulations of global transport of tracer impurity particles using the ASCOT code. For these studies, information is needed regarding plasma conditions during the experiments (the *background plasma*) and, in the case of tracer injections, about the dissociation of the injected molecules resulting in the birth of tracer impurities. As ASCOT is not capable of modelling these phenomena, additional simulation codes are needed to provide input. In the following, a brief introduction is given to the simulation codes employed in this work.

4.1 Plasma conditions

The quantities of interest in this work are density, temperature and the parallel flow velocity of the plasma: $n_{e,i}$, $T_{e,i}$ and $v_\parallel$, respectively. In the core plasma region with closed magnetic flux surfaces, plasma pressure is constant along a flux surface, which effectively enables to treat the core plasma as one-dimensional. Measured 1D profiles of the quantities of interest using standard diagnostics (e.g., Thomson scattering) are thus sufficient to provide a background plasma for simulations in the core plasma.

Along the open magnetic flux surfaces of the SOL plasma, however, significant density and temperature gradients typically exist between the main chamber and the divertor regions. Consequently, realistic description of the SOL plasma conditions necessitates at least two-dimensional treatment. SOL plasmas are commonly modelled using specialised simulation codes.

4.1.1 The two-point model

Although modelling of plasma conditions in the SOL is complex in general, a somewhat simplified approach can be adopted for plasmas in a limiter configuration. In the simplest scenario (the *sheath-limited regime*), the heat arriving from the core plasma to the SOL is assumed to be conducted towards the contact points with the wall resulting in an almost isothermal plasma [24]. This corresponds to low values of collisionality, described by the SOL collisionality parameter [24]

$$\nu^* = \frac{L}{\lambda_{ee}} \approx \frac{n_e L}{10^{16} T_e^2}, \tag{4.1}$$

where L is the magnetic connection length [m] and λ_{ee} the self-collisional mean free path of electrons [m] with n_e in [m^{-3}] and T_e in [eV].

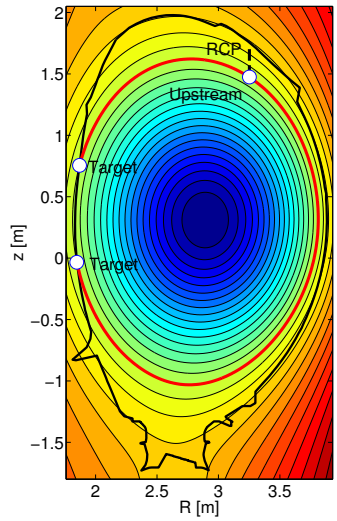

Figure 4.1. Utilisation of the two-point model in creating a background plasma. As the upstream plasma conditions are known based on, e.g., reciprocating probe (RCP) measurements, density and temperature at the target locations can be calculated using the two-point model. Interpolating between upstream and target yields values for an entire magnetic flux surface (red).

In the sheath-limited regime, the *two-point model* can be utilised to relate plasma conditions at the contact point (the *target* location) and away from it along the magnetic field (the *upstream* location). In Publication IV, plasma conditions in an inner-wall limited discharge in JET were sheath-limited thus justifying this method.

In the basic formulation of the two-point model, the upstream (n_u, T_u) and target (n_t, T_t) plasma conditions are connected with the equations [24]

$$2n_tT_t = n_uT_u, \tag{4.2}$$

$$T_u^{7/2} = T_t^{7/2} + \frac{7}{2}\frac{q_\parallel L}{\kappa_{0e}}, \tag{4.3}$$

$$q_\parallel = \gamma n_t k T_t c_{st}, \tag{4.4}$$

where $q_\parallel$ is the parallel power flux density, $\kappa_{0e} \approx 2000$ $\mathrm{Wm^{-1}s^{-1}eV^{-5/2}}$ a coefficient for heat conductivity, $\gamma \approx 7$ the sheath heat transmission coefficient and c_{st} the plasma sound speed at the target.

In this form, the set of equations can be used to calculate upstream conditions when values at the targets are known (from, e.g., Langmuir probe measurements). Reversely, solving for n_t and T_t, target plasma conditions can be determined based on measured upstream values.

Temperature and density values for an entire magnetic flux surface can then be obtained by interpolating between the upstream and target values

along the surface which is illustrated in Figure 4.1. Performing this for a set of magnetic flux surfaces results in a 2D background plasma on the (R,z) plane.

4.1.2 Plasma fluid theory

In a divertor configuration, more sophisticated methods compared to the two-point model are required for a detailed description of SOL plasma conditions. With increasing collisionality ν^*, the SOL plasma enters the *conduction-limited (high-recycling) regime* where the finite conductivity of the plasma restricts heat transfer between upstream and target locations, resulting in a temperature gradient parallel to the magnetic field [24]. As collisionality is increased even further, eroded particles from divertor targets can form a neutral cloud in front of the divertor surface, which suppresses the incoming ion flux and results in pressure losses [24]. In this *detached regime*, very low temperature and density values can be achieved at the divertor targets.

The most common approach for modelling SOL plasmas in the conduction-limited and detached regimes involves plasma fluid theory. Among the most prominent plasma fluid code packages are SOLPS [67] (commonly used for ASDEX Upgrade and ITER) and EDGE2D-EIRENE [68] (the preferred tool for JET). Both code packages share the same structure of coupling a separate fluid code (B2 or B2.5 in SOLPS and EDGE2D in EDGE2D-EIRENE) for the charged plasma to the Monte Carlo code EIRENE [69] for neutrals. These tools were utilised in Publications II–IV to model plasma conditions in divertor configurations in AUG and JET.

A well-known derivation of the plasma fluid equations that serve as a basis for the codes was given by Braginskii [70]. The set of equations, derived by calculating moments of the kinetic Fokker-Planck equation, express the conservation of particles, momentum and energy. For neutrals, the simulation is based on the Boltzmann transport equation.

Plasma solutions from fluid codes typically result from extensive scans in the input parameters done with an aim to reproduce experimentally measured profiles. Of these, heating power arriving to the computational grid and the density level can be approximated from, e.g, experimental data. However, perpendicular transport coefficients (diffusivity $D_\perp$, electron and ion heat conductivities $\chi_{e,i}$) have more of an *ad hoc* nature due to the complexity of the transport phenomena in the SOL as will be further discussed in Section 4.3.3.

The *onion-skin method* (OSM) is another application of plasma fluid theory for modelling plasma conditions [24]. OSM typically utilises a 1D version of the fluid equations that are solved for individual nested flux tubes, i.e., elementary volume elements in the direction parallel to the magnetic field to generate a 2D solution of the SOL plasma. The solutions are obtained based on boundary conditions that commonly consist of radial profiles of temperature and density at the divertor targets. As the boundary conditions constrain the plasma solution radially, prescribed profiles for the perpendicular transport coefficients are not needed as an input for OSM. Instead, it is possible to extract the coefficients from the OSM solution. Due to the required boundary conditions, OSM is mainly used for interpretative studies. In Publication I, an OSM solution from studies preceding this work was employed to provide a background plasma for the simulations in AUG.

Despite its widespread use in fusion research, fluid modelling has been found to suffer from certain weaknesses. Comparing the simulated plasma solutions with experimental measurements (of, e.g., n_e and T_e), obtaining a match simultaneously at an upstream location and the inner and outer divertors is typically challenging, in particular in high-density plasmas [71]. Furthermore, in most cases fluid code solutions seriously underestimate the plasma flow velocity in the main chamber when compared to experimental observations, see, e.g., [72, 73]. Besides the simplified model for radial transport used in fluid codes [74], it has been argued that the problem of flows is partially due to the inability of the codes to correctly model the radial electric field [75, 76]. Additionally, noticeably better agreement with the plasma flow pattern inferred from experimental measurements has been obtained with kinetic simulations that have highlighted the role of trapped ions [77].

Since flows play such a crucial role in impurity migration, these issues have led in some cases to the use of manually imposed more realistic (compared to flow measurements) flow patterns in global impurity transport simulations, even though this violates the self-consistency of the plasma solution. Such work has been done for DIII-D [78, 79] and later also for AUG [80]. This approach will be utilised also in the ASCOT simulations of this work.

4.2 Molecule dissociation

In the case of tracer injection experiments, the migration of impurities starts in a molecular form. The transport and dissociation of the injected molecules determine the birth locations of the tracer ions (such as $^{13}C^{+}$) which then experience migration in the actual plasma.

Simplified estimates of the ion birth locations can be obtained by treating the injected molecules as neutral atoms and calculating their ionisation mean free paths. The birth location can also be left as a free parameter that can be varied. More detailed information regarding the birth of the ions, however, can be obtained with direct simulations of the dissociation chains of the molecules.

Considering, e.g., methane molecules, the reaction chain progressing from $^{13}CH_4$ to $^{13}C^{+}$ can be rather complex. The molecule $^{13}CH_4$ can first be either ionised or it can be dissociated into smaller fragments such as $^{13}CH_3$ or $^{13}CH_2$. These reaction products can again be either neutral or charged which affects their transport. While neutral molecules follow ballistic orbits, transport in a charged state is governed by the magnetic field.

In the context of this thesis, the impurity transport and plasma-surface interaction code ERO [81] was used in Publications II and III to provide the birth distributions of $^{13}C^{+}$ and $^{15}N^{+}$ ions. With ERO, the orbits of the injected molecules can be followed starting from their injection location. As the molecules are transported towards the plasma, the reaction rates for the various possible reactions are constantly updated based on the local plasma conditions given by the background plasma. A Monte Carlo method is then used to determine which reaction, if any, occurs during a time step [82].

In the work presented in Publications II and III, the dissociation chains were simulated until a singly charged ion was born. Finally, basic parameters of the ions – their (R,z) location, energy and direction of velocity – were recorded to be used as input for ASCOT simulations. It should be noticed that there was no coupling between ERO and ASCOT, so that ERO was only used to provide the initial test particle ensembles for ASCOT studies.

4.3 Impurity transport

4.3.1 Single particle motion and guiding-centre formalism

The motion of a single particle in an electromagnetic field (ignoring non-electromagnetic forces) is governed by the Lorentz force as

$$m\frac{\mathrm{d}\mathbf{v}}{\mathrm{d}t} = q(\mathbf{E} + \mathbf{v} \times \mathbf{B}), \tag{4.5}$$

where $\mathbf{v}$ is the particle velocity, q its charge and $\mathbf{E}$ and $\mathbf{B}$ the electric and magnetic fields, respectively. Utilising this basic description for global orbit-following simulations in tokamaks, however, is typically computationally very intensive. Considering the case of $\mathbf{E} = 0$ and a constant, straight magnetic field, the $\mathbf{v} \times \mathbf{B}$ term of Equation (4.5) results in a helical orbit with the particle following a magnetic field line while rapidly gyrating around it. As a consequence of the high gyration frequency (of the order of 0.1 GHz for protons in fusion plasmas), a very small time step is needed for accurate simulations of particle motion.

The motion of the particle can be simplified by separating it into the motion of the centre of gyration (the *guiding-centre*) and the motion around it. This *guiding-centre approximation* is valid as long as the relevant background quantities vary only slowly with respect to the spatial and temporal scales of the gyration. More specifically, for the magnetic field the requirement is

$$r_L \frac{|\nabla B|}{B} \ll 1, \tag{4.6}$$

$$\frac{\Omega}{B}\left|\frac{\mathrm{d}B}{\mathrm{d}t}\right| \ll 1, \tag{4.7}$$

where $r_L = mv_\perp/|q|B$ is the radius of gyration (the *Larmor radius*) and $\Omega = |q|B/m$ the gyration frequency (the *Larmor frequency*). Following the guiding-centre instead of the actual particle offers a significant reduction (even a factor of 100 [83]) in the computational time in simulations as the gyromotion can be ignored.

Besides helical motion, particles in more complex electromagnetic fields are subject to *drifts* that cause transport in the direction perpendicular to the magnetic field. In a non-uniform magnetic field, the field gradient causes the Larmor radius to vary during a single gyration ($r_L \propto 1/B$) which results in the ∇B *drift*. Curvature in the magnetic field results in a similar effect, the *curvature drift*, due to the centrifugal force. These two

drifts can be combined as the $\boldsymbol{B \times \nabla B}$ *drift* with a velocity of [6]

$$\mathbf{v}_{\mathbf{B}\times\nabla B} = \frac{v_{\parallel}^2 + \frac{1}{2}v_{\perp}^2}{\Omega}\frac{\mathbf{B}\times\nabla B}{B^2}. \tag{4.8}$$

As $\Omega \propto q$, the $\mathbf{B} \times \nabla B$ drift separates ions and electrons resulting in an electric field perpendicular to the magnetic field.

The presence of an electric field generates the $\boldsymbol{E \times B}$ *drift* with the velocity [6]

$$\mathbf{v}_{\mathbf{E}\times\mathbf{B}} = \frac{\mathbf{E}\times\mathbf{B}}{B^2}, \tag{4.9}$$

acting independently of the particle charge. Besides these presented drifts, also others exist, such as the polarisation drift due to a non-stationary electric field. In short, the motion of a guiding-centre in an electromagnetic field is thus composed of fast motion parallel to the magnetic field and a slow drift away from it.

In addition to giving rise to drifts, the non-uniformity of the magnetic field also affects the parallel-$\mathbf{B}$ motion. If the electromagnetic fields exhibit only slow variation (recall Equations (4.6) and (4.7)), the magnetic moment

$$\mu = \frac{mv_{\perp}^2}{2B} \tag{4.10}$$

is an adiabatic invariant, i.e., it remains approximately constant [6]. This implies that a particle moving towards a stronger magnetic field $\mathbf{B}$ (e.g., from the LFS to the HFS in a tokamak) will experience an increase in its perpendicular velocity $v_{\perp}$. As the total kinetic energy remains constant, the parallel velocity $v_{\parallel}$ will correspondingly decrease. Moving towards a constantly increasing magnetic field strength, eventually a turning point is reached where $v_{\parallel} = 0$ and the particle experiences reflection. The particle then effectively becomes trapped between two turning points. In a tokamak, due to the influence of the $\mathbf{B} \times \nabla B$ drift at the turning points, trapped particle orbits typically resemble a banana in a poloidal projection.

4.3.2 Transport in a tokamak plasma

In a plasma, particle motion is affected not only by the magnetic field as described in Section 4.3.1 but also by interaction with other particles. As each charged plasma particle is a source to a microscopic electromagnetic field, a particle moving in the plasma experiences *Coulomb collisions* with

particles within its proximity[1].

In addition to changes in the energy and direction of velocity of the particle, collisions also result in spatial motion across the magnetic field lines. This *classical transport* can be treated as diffusion with a step size given by the Larmor radius r_L. More significant cross-field transport effects are due to trapped orbits. If, e.g., a trapped particle is transformed into a passing particle as a result of a collision, it experiences a radial displacement with the size of the width of the banana orbit δ_{r_b}. This width is of the order of $\delta_{r_b} \propto qr_L/\sqrt{\epsilon}$ and exceeds significantly the Larmor radius as q is the safety factor of the magnetic field and $\epsilon = a/R_0$ the inverse aspect ratio of the tokamak. *Neoclassical transport* accounts also for the influence of trapped orbits, and it is stronger than classical transport by an order of magnitude [84].

Experimental studies have indicated, however, that the transport levels observed in tokamaks in reality significantly exceed the neoclassical predictions by factors of 10–100 [85]. The additional transport, often classified as *anomalous transport*, is widely regarded as originating in plasma turbulence [9,85]. Nevertheless, the understanding of plasma turbulence, or any form of turbulence in general, is still incomplete and simulations of turbulence are typically computationally very intensive. Consequently, in orbit-following simulation codes it is common to address the anomalous part of transport by increasing the radial transport of the particles using simplified models. In practice, the standard method is to use a diffusion model with an *ad hoc* coefficient that can be specified or a diffusive-convective model with an additional convection velocity.

Regarding the transport of low-energy impurities in the SOL, two collisional transport phenomena are of particular interest. As already mentioned in Section 2.2, SOL plasmas exhibit strong parallel flows towards the divertor targets. Impurity ions in the SOL become coupled to these flows of the main plasma through collisions. Due to the flow, collisions with the main plasma do not scatter impurity particles isotropically but, instead, deflect their velocities towards the flow direction. The entrainment of impurities by the flow therefore results in transport towards the divertor.

Another collisional phenomenon arises due to temperature gradients

[1] In more rigorous terms, the collisions are due to particles within the plasma Debye length (the Debye sphere). Fields outside this distance are effectively screened as a result of the quasineutrality of the plasma.

along the magnetic field in the SOL. For collisions of the impurities with the main plasma, the collision frequency is inversely proportional to the plasma temperature as $\nu_{e,i} \propto T_{e,i}^{-3/2}$. In the presence of a temperature gradient, an impurity ion consequently experiences more frequent collisions with particles from a lower temperature side than from a higher temperature side. This results in transport towards the direction of a higher temperature, and the effect is commonly referred to as the *temperature gradient force* or the *thermal force* when describing impurity transport in terms of forces [24, 70]. In a divertor configuration, the most significant parallel-B temperature gradients exist near the divertor region with the temperature decreasing towards the divertor targets. Therefore, the resulting transport is towards the main chamber plasma.

In the divertor plasma, plasma flows and temperature gradients thus promote impurity transport in opposite directions along the magnetic field. Nevertheless, in the main chamber region in the SOL, temperature gradients are typically minor and collisional transport is dominated by the flow.

4.3.3 The ASCOT code

Orbit-following of test particles and interactions with the background plasma

ASCOT (**A**ccelerated **S**imulation of **C**harged Particle **O**rbits in **T**okamaks) is a Monte Carlo orbit-following simulation code originally developed in the 1990s as a collaboration between Helsinki University of Technology (currently part of Aalto University) and VTT Technical Research Centre of Finland [86]. Since then, substantial development effort has been conducted both to include additional physics and to adopt modern programming conventions and computational methods [87][2]. In the recent years, the primary applications of ASCOT have been related to the simulation of energetic particles (fusion alphas and NBI ions) in, e.g., ITER (see [14, 88–90]).

The code simulates the orbits of a specified test particle ensemble in a stationary magnetic field and background plasma. One of the main strengths of ASCOT is the capability for 3D simulations as both the mag-

[2]During the course of the work presented in this thesis, a fully re-written version of the code, called ASCOT4, was developed. However, all of the simulations of this thesis employed the preceding ASCOT version (ASCOT3). Also, the description of the code presented here considers ASCOT3.

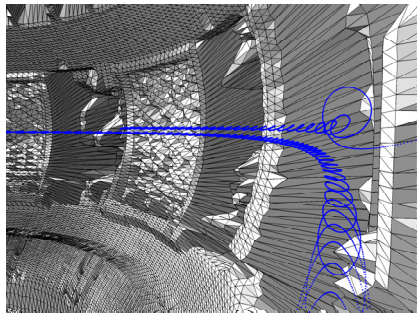

Figure 4.2. Example of a full gyro-orbit of a carbon ion (energy of 1 keV) in ASDEX Upgrade as simulated with ASCOT.

netic field and the wall geometry of the tokamak can be given in a realistic non-axisymmetric form. Furthermore, the test particles can be followed in an unrestricted computational domain ranging from the core plasma to the wall. These features make ASCOT particularly attractive regarding impurity studies as most simulation codes for global impurity transport in the SOL (such as DIVIMP [91, 92]) typically assume an axisymmetric tokamak environment with a restricted computational domain that focuses on the divertor-SOL.

While relying mainly on guiding-centre theory, ASCOT is also capable of following the full gyro-orbits of the particles (see Figure 4.2). Additionally, it is possible to perform guiding-centre following until reaching sufficiently close (with respect to the Larmor radius) to a wall surface after which full gyro-orbit following is used to obtain an accurate location for a collision with the wall [83].

In ASCOT, guiding-centre following is based on equations of motion derived using the Hamiltonian formalism which can be expressed for the gyro angle χ, magnetic moment μ, and the parallel velocity and the position of the guiding-center, $v_\parallel$ and $\mathbf{R}$, as [87]

$$\dot{\chi} = \frac{qB}{m}, \tag{4.11}$$

$$\dot{\mu} = 0, \tag{4.12}$$

$$\dot{v_\parallel} = \frac{q}{m}\frac{\mathbf{B}^*}{B^*_\parallel} \cdot \mathbf{E}^*, \tag{4.13}$$

$$\dot{\mathbf{R}} = v_\parallel \frac{\mathbf{B}^*}{B^*_\parallel} + \mathbf{E}^* \times \frac{\mathbf{b}}{B^*_\parallel}, \tag{4.14}$$

with $\mathbf{B}$ being the magnetic field unit vector. Here, $B^*_\parallel = \mathbf{B}^* \cdot \mathbf{B}$ and the effective fields $\mathbf{E}^* = \partial \mathbf{A}^*/\partial t - \nabla \Phi^*$ and $\mathbf{B}^* = \nabla \times \mathbf{A}^*$ are defined by their

effective potentials

$$\Phi^*(\mathbf{R}, \mu, t) = \Phi + \mu B/q, \tag{4.15}$$

$$\mathbf{A}^*(\mathbf{R}, v_\parallel, t) = \mathbf{A} + m v_\parallel \mathbf{b}/q. \tag{4.16}$$

Advancing the equations of motion in time is done using a Runge-Kutta method.

The influence of Coulomb collisions is evaluated using Monte Carlo operators for the particle pitch $\xi = v_\parallel/v$ and energy E [93]. When considering impurity transport in the SOL, it should be noticed that these operators are derived based on the assumption of a purely Maxwellian background plasma. While this is a reasonable approximation for the core plasma, the operators neglect the influences of plasma flow and parallel-$\mathbf{B}$ temperature gradients (Section 4.3.2) that are of importance for impurity transport in the SOL.

In ASCOT, the effect of plasma flow on collisions can be included by evaluating the collision operators in a moving frame of reference. When the flow velocity at the current location is known, the parallel velocity is transformed as $v'_\parallel = v_\parallel - v_{\text{flow}}$ and other quantities such as pitch are updated accordingly. The collision operators are then evaluated in their usual manner, after which the quantities are transformed back into the original frame of reference.

The influence of parallel-$\mathbf{B}$ temperature gradients, however, is neglected in the current version of the code as accounting for it rigorously would require either re-derivation of the collision operators, or adopting entirely new operators as presented in, e.g., [94]. Consequently, ASCOT simulations of impurity transport are best applicable to scenarios where transport parallel to the magnetic field in the SOL is dominated by the flow. As discussed in Section 4.3.2, this holds for the main chamber plasma where the temperature gradients are only minor and, in contrast, flows very strong. The neglection of these gradients in collisions therefore arguably results only in a potential overestimation of divertor deposition in ASCOT results.

In addition to neoclassical transport, anomalous radial transport can be included in ASCOT using a diffusion operator with a diffusion coefficient $D_\perp^{\text{imp}}$. Regarding fast ions, a theoretical model for the diffusion coefficient has been developed [95] and included in ASCOT [88]. However, for impurities a corresponding model has not been encountered and, consequently, $D_\perp^{\text{imp}}$ is set to a constant *ad hoc* value in simulations.

In the case of impurities, the charge state q of the particles can vary substantially due to ionisation and recombination. In ASCOT, the influence of these atomic processes is included with a probabilistic model [87]. Based on cross section data from the ADAS database [96], the model calculates the probabilities for effective ionisation ($q \rightarrow q + 1$) and effective recombination ($q \rightarrow q - 1$) during a timestep. A Monte Carlo method is then applied to determine whether one of these outcomes occurs or whether the charge state remains unchanged. If recombination results in a neutral particle, its ballistic orbit is followed until ionisation. As the model considers *effective* ionisation and recombination, it does not provide information regarding which individual atomic processes are experienced by the particle and, hence, merely follows the changes in the charge state.

It should be noticed that ASCOT simulates only the transport of the impurities, from a given initial state typically until an impact with the wall which is assumed to lead to deposition. The subsequent erosion, transport and re-deposition of the deposited particles (Section 2.2) are thus not modelled. Consequently, when performing comparisons to experimental results, the emphasis in this work is on large-scale impurity deposition, i.e., comparing fractions of particles deposited in different poloidal regions. In the case of tracer injection experiments on AUG, erosion arguably does not substantially impact large-scale deposition due to the rather short time scales. In, e.g., 2011 the total flattop time during the experiment was around 53 s.

Inputs for simulations

For simulating impurity transport during an actual plasma discharge, ASCOT needs to be provided with information regarding the tokamak magnetic field, background plasma and wall geometry as an input. For the magnetic field, the axisymmetric (2D) equilibrium field is routinely created for each discharge on, e.g., AUG and JET using Grad-Shafranov solvers such as CLISTE [97] and EFIT [98]. This can be utilised as an axisymmetric magnetic field in ASCOT or extended to account for 3D effects, mainly toroidal field ripple and resonant magnetic perturbations.

The inclusion of these features relies on the vacuum approximation which assumes that an external magnetic perturbation can be superposed onto the 2D equilibrium field to obtain the total magnetic field. While commonly used due to its simplicity, the plasma in reality creates a response to the applied perturbation which can partially shield its effect. Plasma

response is prominent in particular with RMPs and it can be modelled with magnetohydrodynamic (MHD) simulations [99].

Toroidal field ripple can be introduced to the magnetic field when the magnetic field resulting from a single toroidal field coil is known. The variation of this toroidal field from its toroidal average ($B_\phi - \overline{B_\phi}$) can then be superposed onto the equilibrium field to obtain a magnetic field with toroidal field ripple. In this process, the contribution of a single coil is duplicated N_{coils} times around the torus with N_{coils} being the number of TF coils in the tokamak.

For a magnetic field with resonant magnetic perturbations, the individual magnetic fields from the RMP coils of a tokamak can be combined with the 2D equilibrium field. Different RMP field configurations (currents in the coils) can be generated by using scaling factors when combining the individual fields.

The background plasma for ASCOT can be given as a 1D profile, in 2D, or the code can be provided with both 1D (core plasma) and 2D (SOL) background plasmas with an operational boundary at the core-SOL interface. Measurements using standard diagnostics can be used to create the 1D profiles for the core plasma, whereas description of the SOL region requires simulations, typically employing plasma fluid codes (Section 4.1).

Besides reproducing experimentally measured plasma conditions with fluid codes, an additional challenge for ASCOT simulations is that the computational grid of the codes is typically restricted and does not extend to the main chamber wall. While recent development has allowed extended computational grids in, e.g., SOLPS [100], they are yet to become a part of routine use.

In the work presented in this thesis, the plasma solutions (using standard computational grids) have consequently been extrapolated as exponentially decaying up to the wall. More specifically, e.g., electron density is extrapolated as

$$n_e(R,z) = n_e^{\mathrm{NN}} \exp(-D/\lambda_{n_e}), \tag{4.17}$$

where n_e^{NN} denotes the value at the nearest neighbour of the edge of the computational grid, D the distance to this location and λ_{n_e} the decay length. The decay lengths can estimated by performing exponential fits to, e.g., Langmuir probe measurements of the far-SOL region. Based on experimental studies of far-SOL plasma conditions on, e.g., DIII-D [101], exponential decay can provide a reasonable approximation at least for the low-field side.

For evaluating collisions of the followed particles with plasma-facing components (i.e., their deposition), ASCOT also requires a (2D or 3D) description of the tokamak wall geometry as an input. In this work, the 3D wall geometries of ASDEX Upgrade and JET are based on computer-aided design (CAD) data of the devices. However, as the raw CAD data is extremely detailed and includes even structures not in contact with the plasma, ray-tracing and smoothing on the data was performed with a method described in [102] to extract only the plasma-facing components with a desired level of detail.

5. Simulations of global impurity transport in ASDEX Upgrade and JET

In this Chapter, an outline of the work carried out for Publications I–IV is presented together with the main results. Firstly, the studies of the ^{13}C and ^{15}N tracer injection experiments on ASDEX Upgrade, resulting in Publications I–III, are presented in Sections 5.1–5.3. Section 5.4 then considers the simulations of ^{10}Be transport in JET which is the subject of Publication IV.

5.1 The effect of non-axisymmetric wall geometry on ^{13}C transport

The ASCOT simulations presented in Publication I considered the ^{13}C injection experiment conducted in 2007 on ASDEX Upgrade (Section 3.1.2). The studies aimed at clarifying the experimental results, most notably the toroidally integrated ^{13}C deposition of less than 10 % of the amount of injected atoms. In particular, attention was directed towards investigating the potential toroidal asymmetry in the ^{13}C deposition pattern.

DIVIMP simulations [80] of the same experiment were used as a basis for the ASCOT studies. Thus, the background plasma of [80], created using the onion-skin method for the discharge #22575, was imported as the background plasma also for the ASCOT simulations. In the far-SOL and halo plasma regions outside the OSM computational grid, the plasma solution was extrapolated as exponentially decaying. As only weak SOL flow was predicted by OSM, a manually imposed flow pattern with a Mach number of 0.5 in the main chamber was used with a stagnation point between the outer midplane and the lower X-point (Figure 2.1).

The magnetic field was based on the 2D equilibrium field of the same discharge at 2.8 s and was amended with toroidal field ripple using the method described in Section 4.3.3. For the wall geometry, a realistic 3D description of ASDEX Upgrade derived from CAD data was used. Based

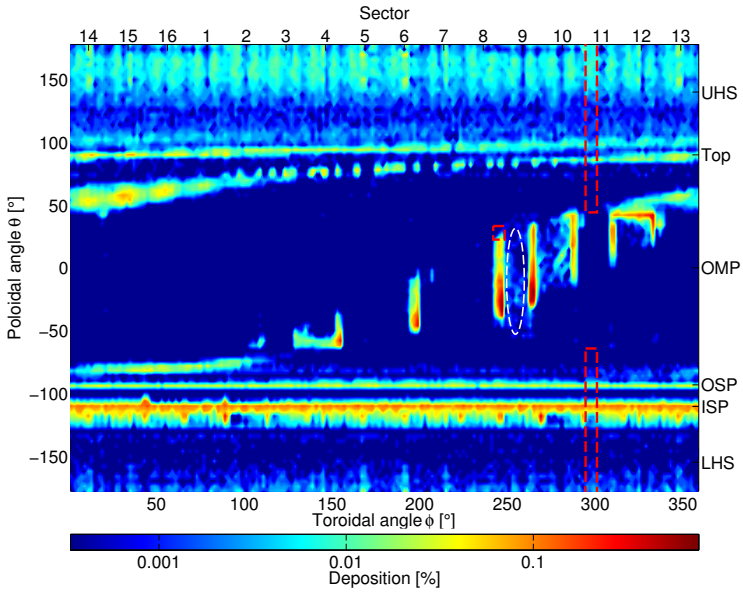

Figure 5.1. Deposition of ^{13}C (on a logarithmic scale) in ASDEX Upgrade as simulated with ASCOT. The indicated poloidal regions are the upper and lower parts of the inner-wall heat shield (*UHS* and *LHS*, respectively), top of the vessel (*Top*), outer midplane (*OMP*) and the inner and outer strike points (*ISP* and *OSP*, respectively). The red dashed rectangles show the regions inside which wall tiles were removed for post mortem analysis, and the injection port location is indicated by the ellipse.

on the DIVIMP simulation results, an anomalous radial diffusion coefficient of $D_{\perp}^{\mathrm{imp}} = 0.25$ m^2/s for the followed impurities was chosen.

Neither experimental data nor simulation results was available regarding the dissociation of the injected $^{13}CH_4$ molecules at the time of Publication I and, hence, the initial distribution of the $^{13}C^+$ ions had to be approximated. Resembling a particle cloud resulting from the dissociation, 300 000 test particles were given a random position over a cylindrical volume ranging from the separatrix 5 cm towards the outer wall (the injection port). The initial energy was set to $E_0 = 0.3$ eV (average Franck-Condon energy of CH molecules) and a random uniform pitch distribution was used, corresponding to an isotropic distribution for the initial velocity.

The transport of the ^{13}C test particles was simulated with ASCOT until their deposition on the wall. Investigating the 2D distribution of deposited ^{13}C revealed that the deposition pattern features substantial toroidal asymmetry at the outer wall (Figure 5.1). The non-axisymmetric nature of the outer wall of ASDEX Upgrade, resulting from, e.g., individual limiters, caused the deposition to be highly localised on these protruding

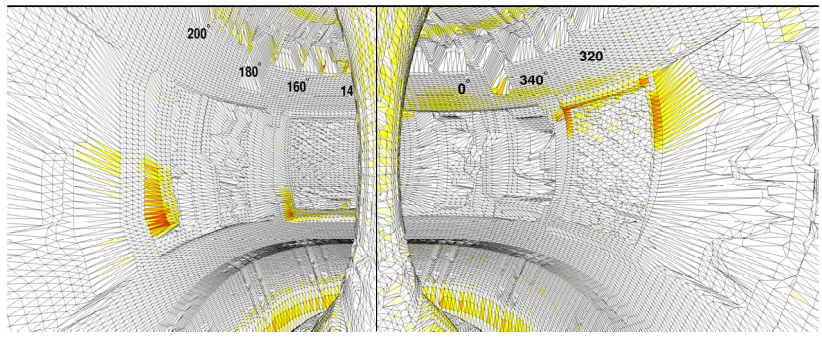

Figure 5.2. Three-dimensional representation of ^{13}C deposition of Figure 5.1 in toroidal sectors 4–6 (left) and 12–13 (right). Highly localised deposition can be observed on a limiter and two ICRH antennas.

structures, prominently visible in Figure 5.2. This effect was particularly strong near the injection location, located between a limiter and an ICRH antenna.

In contrast, according to the simulations deposition on other parts of the torus, i.e., the top of the vessel, inner-wall heat shield and the divertor region, was rather symmetric toroidally. The assumption of toroidally symmetric ^{13}C deposition was therefore considered justified in these regions whereas at the outer wall it was predicted to be invalid.

A significant observation was also that despite large changes in the simulation parameters, the toroidal asymmetry at the outer wall was a robust part of the deposition pattern. While varying the initial spatial distribution of ^{13}C, the initial energy E_0 (between 0.1 and 20 eV), the diffusion coefficient $D_\perp^{\mathrm{imp}}$ (0.1–1.0 m^2/s) and the flow pattern (imposed or OSM solution) had an impact on the deposition, this did not cancel the strong effect of the non-axisymmetric wall geometry.

Considering the experimental results, the ASCOT simulations suggested that the toroidally asymmetric deposition pattern could be one of the explaining factors for the extremely low toroidally integrated ^{13}C deposition. The experimental estimate of outer wall deposition was based on only a single wall tile (Figure 5.1) removed for post mortem analysis from the limiter neighbouring the injection port. According to the simulations, the tile was away from the regions of highest deposition and, thus, the toroidal integration could leave even 30 % of deposited ^{13}C unaccounted for.

The primary conclusion from Publication I was that, in contrast to typical assumptions, the deposition pattern of ^{13}C showed strong signs of toroidal asymmetry. From the modelling point of view, it was seen that

the capability of ASCOT for 3D simulations in an unrestricted computational domain can be a substantial asset for improving the understanding of the experimental results. The work encouraged to study the predicted toroidal asymmetry also experimentally and to continue using ASCOT to aid the interpretation of these studies.

5.2 Studies of molecule dissociation and plasma conditions

The second tracer injection experiment, carried out on AUG in 2011 (Section 3.1.2), was the focus of extensive modelling efforts using SOLPS, ERO and ASCOT, as reported in Publication II. These studies were aimed at several different topics. Firstly, as the dissociation of the injected molecules remained poorly understood, dedicated ERO simulations were prepared to provide the $^{13}C^{+}$ and $^{15}N^{+}$ birth distributions resulting from the dissociation to be used as input for ASCOT. Both the ERO and ASCOT studies were performed for a set of background plasma solutions from SOLPS, trying to identify the role of plasma conditions on the deposition patterns. Finally, as both ^{13}C and ^{15}N were studied, it was possible to compare impurity transport between these particle species.

The SOLPS simulations considered plasmas with electron density at the outer midplane separatrix ranging between 1.0 and 3.0×10^{19} m^{-3}. The power coming from the core plasma to the edge of the SOLPS computational grid, P_{in}, was correspondingly varied between 1.0 and 3.0 MW. Following the description of Section 4.2, both $^{13}CH_4$ and $^{15}N_2$ molecules were then simulated with ERO for each of the SOLPS cases all the way from the injection valve to the plasma until singly charged ions were reached in the dissociation chains. For the background plasmas for ERO, the SOLPS plasma solutions were extrapolated as exponentially decaying up to the injection port, with decay lengths based on experimental measurements. The weak background plasma flow predicted by SOLPS was overwritten with an imposed flow pattern of Mach 0.5 in the main chamber, as in Publication I.

The ERO simulations indicated wide radial profiles for the born $^{13}C^{+}$ and $^{15}N^{+}$ ions, extending from the separatrix several centimetres into the far-SOL and halo plasma (Figure 5.3(a)). With increasing density, the profiles are shifted away from the separatrix towards the outer wall by even centimetres. In all cases, a significant, even dominant part of the dissociation occurs outside the divertor-SOL which is not part of the computa-

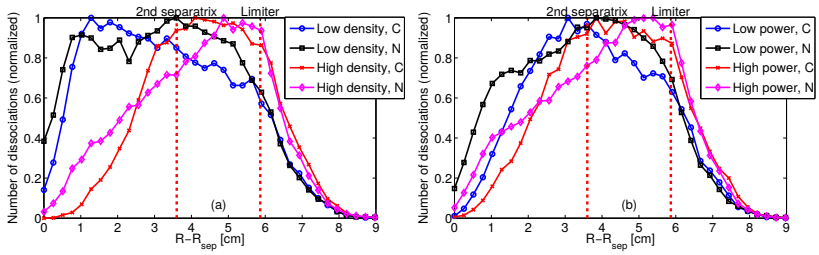

Figure 5.3. Radial birth profiles of $^{13}C^{+}$ and $^{15}N^{+}$ ions as simulated with ERO for increasing (*a*) density and (*b*) heating power.

tional domain in various SOL plasma simulation codes. Furthermore, no major differences can be seen between the profiles for carbon and nitrogen despite the different structure of the $^{13}CH_4$ and $^{15}N_2$ molecules.

Similarly as for increasing density, also increasing heating power was seen to result in a radial displacement of the profiles towards the outer wall, although the effect of heating power was considerably weaker (Figure 5.3(*b*)). As similar observations were made for both carbon and nitrogen, the ERO simulations indicated the dissociation of methane and nitrogen molecules to be largely similar in the studied scenarios.

For the most accurate possible description of plasma conditions near the injection location, an additional background plasma (labelled *Exp. data* in the following) was also created for ERO based on experimentally measured 1D profiles of n_e and T_e near the outer midplane. To obtain a 2D background plasma, these profiles were mapped to magnetic flux surfaces assuming negligible gradients parallel to the magnetic field. Using this background plasma in ERO resulted in $^{13}CH_4$ and $^{15}N_2$ dissociation even closer to the injection location than in the shown profiles (Figure 5.3(*a*) and (*b*)).

ASCOT simulations were carried out with the magnetic equilibrium field from the AUG discharge #27385 at 4.0 s amended with toroidal field ripple as described in Section 4.3.3. As for ERO, the SOLPS plasma solutions were used as the basis for the background plasma in the SOL. Following the simulation setup of Publication I, a 3D wall geometry of AUG was used in the simulations and the anomalous radial diffusion coefficient was initially set to $D_{\perp}^{\mathrm{imp}} = 0.25$ m^2/s. To account for changes in the AUG vessel between 2007 and 2011, the wall geometry was updated with the latest CAD data.

The ERO predictions of $^{13}C^{+}$ and $^{15}N^{+}$ birth distributions were used to create the initial test particle ensembles for ASCOT by using the simu-

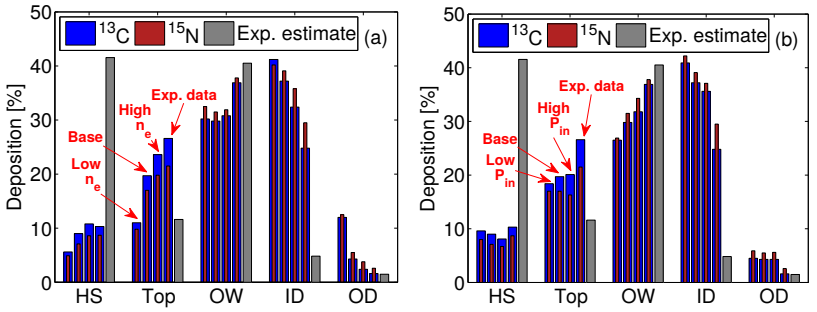

Figure 5.4. Large-scale deposition of ^{13}C and ^{15}N as simulated with ASCOT with increasing background plasma (*a*) density and (*b*) heating power. The poloidal regions are the same as in Table 3.2. Experimental estimate for ^{13}C is shown in grey.

lated values for the initial energy of the particles, their pitch and (R,z) position. As the output from ERO considered only the (R,z) plane in 2D, the particles were assumed to follow a uniform toroidal distribution within the toroidal extent of the injection port. This assumption is justified, e.g., based on experimental observations of the injection of deuterium gas from the same location.

The ASCOT simulation results showed qualitatively similar deposition patterns as in Publication I. At the outer wall, highly localised deposition appeared on the protruding wall structures whereas in other parts of the vessel deposition was rather symmetric toroidally. With varying plasma conditions, however, considerable changes were observed in large-scale deposition in different poloidal regions. Both with increasing density (Figure 5.4(*a*)) and heating power (Figure 5.4(*b*)), deposition in the main chamber was observed to increase and, correspondingly, to decrease at the divertor region. Similar observations were made both for ^{13}C and ^{15}N, and only minor differences were encountered in the deposition patterns between the particle species. Therefore, the transport of carbon and nitrogen was predicted to be largely similar.

Plasma conditions influence the simulated deposition patterns in two primary ways. Firstly, the magnetic topology (in particular in the magnetic configuration of the experiment) varies in the radial direction in the SOL. Near the separatrix, magnetic flux surfaces connect the inner and outer divertor targets, whereas radially further away, such as in the far-SOL, the flux surfaces can remain completely outside the divertor region. As the dissociation of the injected molecules was seen to be strongly dependent on plasma conditions, the radial dissociation location plays a key

role in determining the ratio between main chamber and divertor deposition.

Secondly, plasma conditions also affect the transport of the tracer ions. In particular, changes in plasma density and temperature influence the collisionality of the ions which can be described by the SOL collisionality parameter $\nu^* \approx n_e L/(10^{16} T_e^2)$ (recall Equation 4.1). Collisionality then determines, among others, the strength of coupling to the background plasma flow which is of fundamental importance for the transport of the ions.

Additionally, main chamber deposition is also influenced by radial transport in the SOL which is dependent on plasma conditions. Studies on Alcator C-Mod L-mode plasmas have indicated that radial transport increases with both collisionality and distance from the separatrix [103]. Therefore, a high-density scenario would imply stronger radial transport for the tracer ions compared to a low-density scenario due to the higher collisionality and the molecule dissociation occurring further away from the separatrix. This indicates even stronger main chamber deposition, as was also confirmed with ASCOT by varying the value for $D_\perp^{\mathrm{imp}}$ between 0.25 and 2.0 m^2/s. In practice, any choice of a constant $D_\perp^{\mathrm{imp}}$ is thus always a compromise, and a radial profile for the coefficient would capture the variation in radial transport better.

Experimentally, the dominant regions for tracer deposition were observed to be in the main chamber, in contrast to the experiment in 2007 as discussed in Section 3.1.2. The results of Publication II suggest that this is a consequence of the increased plasma density compared to 2007, affecting both the dissociation of the molecules and the transport of the tracers. With increasing density, changes in the dissociation location and the radial transport were observed to promote higher main chamber deposition. Nevertheless, it should be noted that the experiments had differences also in, e.g., the magnetic configuration.

Although modelling of the experiment indicated no noticeable differences in neither the dissociation of the molecules nor the transport of the tracers when comparing carbon and nitrogen, the final deposition patterns are determined also by plasma-surface interaction. An important experimental observation (recall Section 3.1.2) was that there were substantial differences between ^{13}C and ^{15}N deposition, and orders of magnitude variations were measured in local surface densities (at/cm^2) between the species. This difference is arguably due to a saturation phenomenon

that has been seen in the interaction of nitrogen particles with a tungsten substrate [104, 105]. In studies on ASDEX Upgrade, nitrogen implantation and deposition on tungsten has been observed to occur only until reaching a saturation concentration. Incoming particle flux towards a saturated surface then mainly experiences reflection which substantially influences the final deposition pattern of nitrogen.

In terms of impurity migration in general, one of the main messages in Publication II is that the penetration depth of erosion products into the plasma can substantially influence whether their transport is directed towards the main chamber or the divertor. Furthermore, plasma-surface interaction was concluded to be capable of substantially modifying the final deposition pattern (even over short time scales of the order of tens of seconds), with this interaction being also strongly dependent on impurity species.

5.3 Influence of TF ripple and RMPs

Although most of the analysis of impurity migration in the SOL does not consider the non-axisymmetric nature of the magnetic field, the 3D features are always present in tokamaks and will likely become increasingly important in ITER with, e.g., the inclusion of resonant magnetic perturbations (Section 1.2.3). In Publication III, ASCOT simulations were performed to elucidate the role of non-axisymmetric features of the magnetic field on impurity transport. As modelling of SOL plasmas is commonly carried out using simulation codes with axisymmetric magnetic fields, the work also aimed at assessing the validity of this axisymmetric assumption in simulations.

The studies were done based on the modelling framework created for Publication II and thus addressed the scenario of the tracer injection experiment of 2011. The ASCOT studies compared simulation cases with (1) an axisymmetric magnetic field, (2) an axisymmetric field with TF ripple and (3) an axisymmetric field with RMPs. Although RMPs were not included in the actual experiment, investigating their influence on impurity migration is important regarding next-step devices.

The background plasma for the SOL was based on a SOLPS solution with a power level of $P_{\mathrm{in}} = 1.6$ MW and an electron density of $n_{e,\mathrm{sep,OMP}} = 2.25 \times 10^{19}$ m^{-3} that was extrapolated to extend to the wall as in Publications I and II. Only ^{13}C transport was simulated, and the $^{13}C^{+}$ ions

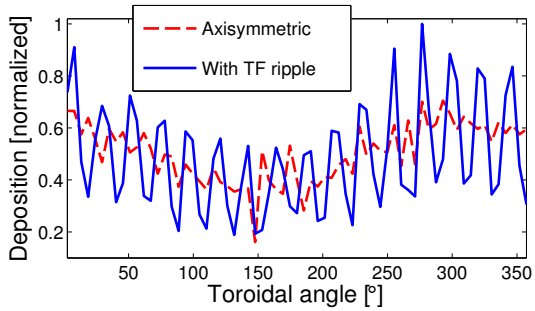

Figure 5.5. Deposition of ^{13}C at the top of the vessel as simulated using ASCOT with and without TF ripple in the magnetic field. Noticeable 16-fold periodicity can be observed in the presence of ripple.

were initialised according to the ERO simulation of $^{13}CH_4$ dissociation on the background plasma employing experimentally measured profiles. The same setup as in Publication II was utilised, including the imposed background plasma flow of Mach 0.5 in the main chamber.

Besides the axisymmetric magnetic field and the field with toroidal field ripple that were available from the simulations presented in Publication II, additional magnetic fields with RMPs were created with different coil configurations based on the vacuum approximation (Section 4.3.3). The fields with RMPs were based on the initial in-vessel coil setup of AUG with four toroidally separated coils above the outer midplane and four below it [17]. Using a coil current of 1 kA in five turns, four different coil configurations were studied, labelled as $++$, $+-$, $-+$ and $--$. Here, the signs denote the direction of current in the coils above and below the outer midplane, respectively, at a toroidal position of reference with toroidally neighbouring coils carrying opposite currents. Each of the active in-vessel coils produces a magnetic field which is mainly radial. For a positive current, this field is towards the plasma and with a negative current towards the wall.

Comparing the ASCOT simulation results of the ^{13}C deposition pattern between the axisymmetric case and the case with TF ripple included, no substantial changes were observed on a global scale. Thus, considering the large-scale deposition in different poloidal regions (e.g., the fraction of particles transported to the inner divertor), the results remained largely unaffected by TF ripple.

Nevertheless, on a local scale ripple induced periodicity into the deposition pattern on the low-field side. This is exemplified by the deposition profile for the top of the vessel (Figure 5.5), exhibiting 16-fold periodicity

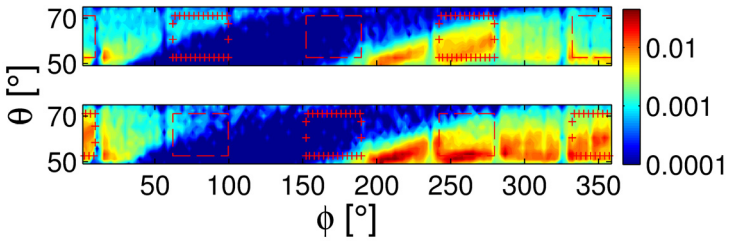

Figure 5.6. Deposition (% of total) of ^{13}C around the upper in-vessel coils as simulated with ASCOT in $+-/++$ (top) and $-+/--$ (bottom) coil configurations. Rectangles indicate the locations of the active in-vessel coils with either positive ($+$ markers) or negative (dashed) currents. The deposition pattern was observed to be independent of the current in the lower set of coils.

corresponding to the number of toroidal field coils in AUG. Locally, it can be seen that ripple results in up to 40 % changes in deposition.

With TF ripple, the magnetic field strength varies in the toroidal direction being highest at the coils and lowest between two adjacent coils. Consequently, magnetic field lines bend outwards (Figure 1.3) in regions between the coils (similarly as in, e.g., a magnetic mirror). Taking into account only this effect and ignoring, e.g, the influence of wall geometry, periodic deposition at the wall is expected with highest deposition in regions between the coils. Furthermore, the presence of ripple also creates ripple-trapped particles, i.e., particles oscillating between two coils due to the varying magnetic field strength.

However, the non-axisymmetric features of the wall geometry can dominate over the influence of TF ripple on the deposition pattern. Therefore, although ripple is strongest around the outer midplane, no substantial periodicity was observed in this region in the simulations as the deposition is localised on the protruding wall structures such as limiters (Figure 5.2).

Similarly as for TF ripple, also in the presence of RMPs the large-scale global deposition was observed to remain unchanged compared to the axisymmetric case, whereas locally the perturbation fields had a prominent effect. In the vicinity of the active in-vessel coils, a local increase (negative current) or decrease (positive current) of ^{13}C deposition was observed, depending on the coil current (Figure 5.6). The radial magnetic fields generated by the coils therefore effectively create either an attractive or repulsive influence on the particle orbits.

Neither TF ripple nor RMPs were therefore seen to affect the global deposition pattern of ^{13}C as simulated with ASCOT. Thus, according to these predictions, the assumption of an axisymmetric magnetic field in

numerical simulations of impurity transport is justified if the studies address only large-scale deposition. Yet, regarding local studies, the non-axisymmetric features of the magnetic field had a significant impact on deposition in specified regions on the low-field side.

In particular with respect to RMPs, it should be emphasised that the results of Publication III are preliminary in the sense that only changes in the magnetic field were considered, and also plasma response was disregarded. Extensive and more detailed modelling of SOL plasmas in the presence of RMPs has been carried out for, e.g., DIII-D [106, 107] and AUG [108] with the 3D plasma fluid code package EMC3-EIRENE [109]. These studies have indicated the appearance of additional effects such as helical plasma flow channels that could further influence impurity migration.

Nevertheless, assuming that the employed simplifications do not result in drastic qualitative changes in the simulation results, the conclusions from Publication III are remarkable. At least in scenarios resembling the one presented here, the results suggest that local-scale studies should account for the non-axisymmetric nature of both the wall geometry and the magnetic field of the tokamak for realistic representations of impurity deposition patterns.

5.4 Global transport of eroded ^{10}Be

In Publication IV, ASCOT was utilised for impurity transport studies in JET. The simulations addressed the ^{10}Be marker tile experiment described in Section 3.2.2. Although also in these studies ASCOT was used to simulate the global transport of tracer impurities and their subsequent deposition, the scenario was substantially different compared to the AUG experiments in several ways. Firstly, the simulations were performed before any experimental measurements of ^{10}Be deposition were available and gave thus only predictive information regarding the deposition pattern. Additionally, the studies addressed a campaign-integrated experiment and, hence, the main focus in the ASCOT simulations was to provide a qualitative picture of ^{10}Be migration. Finally, besides migration in a diverted plasma, also the limiter configuration was important to include in the analysis of the experiment due to the location of the ^{10}Be marker tile assembly at the inner wall (Section 3.2.2).

The aim in the ASCOT simulations was to determine the dominant mi-

gration pathways for the eroded ^{10}Be and, thereby, to predict potentially interesting regions for post mortem analysis. Furthermore, as the realistic 3D wall geometry had been observed to have a significant impact on the ^{13}C deposition pattern on ASDEX Upgrade, this study provided an opportunity to test if similar characteristics of toroidal asymmetry could be seen also on JET.

The ASCOT studies considered a scenario where the ^{10}Be marker is subject to physical sputtering during an inner-wall limited plasma start-up phase which was expected to lead to high erosion. The simulations were then continued in a diverted plasma to investigate migration during a subsequent flattop phase. For an accurate presentation of the deposition pattern, a 3D wall geometry was created utilising ray-tracing on CAD data of JET in its latest ITER-like wall configuration.

For the limiter configuration, the simulations addressed the JET pulse number 80836 [110] and utilised the magnetic equilibrium field at 56 s. The background plasma for the SOL was created based on the two-point model (recall Section 4.1.1) and using reciprocating probe measurements of n_e, T_e and $v_\parallel$ as an input.

The studied diverted plasma was JPN 80295, and a magnetic equilibrium of the discharge at 59 s was provided as an input for ASCOT. The SOL background plasma was based on an EDGE2D-EIRENE solution [111] that was extended to the wall with exponentially decaying profiles (with decay lengths obtained from experimental data) in a similar manner as for the ASDEX Upgrade plasmas in Publications I–III. Both in the limiter and the divertor configurations, experimentally measured profiles using high-resolution Thomson scattering of n_e and T_e were used for the background plasma in the core region.

Test particles for the limiter plasma were initialised by calculating ionisation mean free paths for ^{10}Be neutrals sputtered from the marker tile. The neutrals were assumed to have an energy of $E_0 = E_B/2 = 1.155$ eV, where E_B is the binding energy of beryllium. The ^{10}Be$^+$ ions were then simulated until either they were deposited on the wall or their maximum simulation time $t_{\max}$ had been reached. For each test particle, the maximum simulation time was taken from a random uniform distribution $t_{\max} \in [10^{-5}, 0.1]$ s and thus the test particle ensemble represents ^{10}Be that is eroded during 0.1 s before the formation of the X-point. The coefficient for anomalous radial diffusion was set to $D_\perp^{\mathrm{imp}} = 1.0$ m^2/s.

In the limiter configuration, the ^{10}Be neutrals can easily penetrate into

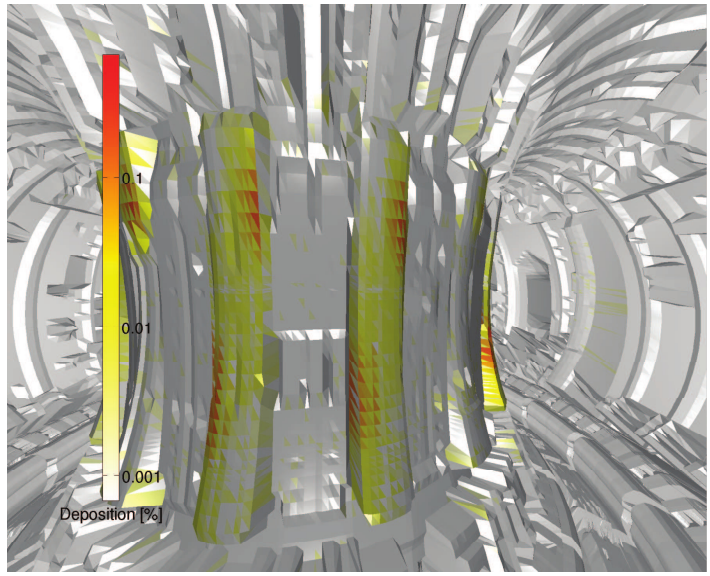

Figure 5.7. Deposition of ^{10}Be during the inner-wall limited plasma phase as simulated with ASCOT. A distinct deposition pattern can be seen on the inner-wall guard limiters with localised deposition on the top right and lower left edges.

the core plasma. The subsequently ionised particles diffusing out of the core into the SOL region were observed to be strongly transported back towards the inner wall along with the plasma flow. As visualised in Figure 5.7, this resulted in a distinct deposition pattern on the IWGLs, with strong and localised deposition on the top right and lower left edges, corresponding to particles arriving from positive and negative toroidal directions and striking the inner wall at these positions. These same regions on the IWGLs have been observed to be net deposition regions in post mortem studies during previous experimental campaigns (employing a carbon wall) on JET [112]. However, the origin of this deposition pattern was not fully understood at the time [113].

As can be seen in Figure 5.8, some of the eroded ^{10}Be is also deposited locally around octant 5 where the marker tile is located. Furthermore, as certain IWGLs (on octants 1–3 and 5–7) are more recessed with respect to the others, only the most protruding limiter structures receive noticeable deposition. Outside the inner wall the deposition of ^{10}Be was predicted to be negligible in the simulated scenario.

Particles that met their maximum simulation time during the limiter phase remained scattered in the core plasma. The simulation of these particles was continued directly from their end state in the diverted phase.

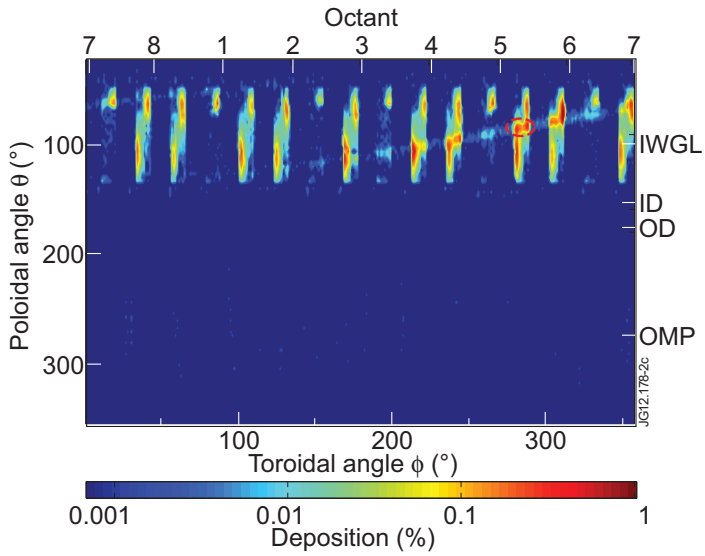

Figure 5.8. As Figure 5.7 but as a 2D distribution. Toroidally, ^{10}Be deposition can be seen to be strongest in the vicinity of the marker tile (red ellipse, octant 5) in octants 4–7.

To get indication of how erosion affects the deposition pattern, the particles that were deposited during the limiter phase were considered to be sputtered, and their simulation was similarly continued in the diverted phase. In the diverted phase, all test particles were then simulated until their deposition on the wall.

As the simulation was continued in the diverted plasma, the particles diffusing out of the core plasma were seen to be deposited mainly on the protruding structures of the outer wall and on the outer divertor. The beryllium that was deposited during the limiter phase predominantly experienced local re-deposition and transport towards the inner divertor aided by the background plasma flow.

The ASCOT simulations therefore predicted that in the case of erosion during an inner-wall limited plasma, ^{10}Be is primarily distributed on the IWGLs from where the particles can further migrate towards the inner divertor. Although the marker tile is both poloidally and toroidally localised, transport in the core plasma results in ^{10}Be deposition over the entire inner-wall region. An additional consequence of core plasma transport is that it enables the particles to be transported also to the low-field side of the vessel, mainly during diverted operation. In a similar manner as for the AUG simulations in Publications I–III, the impurity deposition pattern was observed to strongly reflect the non-axisymmetric nature of

the wall geometry.

It should be stressed that the results of Publication IV were primarily qualitative as only two discharges were analysed from a campaign-integrated experiment and the erosion of deposited particles was not properly accounted for. Still, the simulations were capable of providing a picture of the ^{10}Be deposition pattern in the entire torus, taking into account the true wall geometry of JET which aids the interpretation of the post mortem results.

After the 2011–2012 experimental campaign, surface analysis of the JET wall tiles was started and the first experimental results of ^{10}Be deposition on the IWGLs were compared to ASCOT predictions from the limiter phase [63, 114]. These experimental results consisted of individual measurement points from the inner-wall guard limiter where the marker tile was located (octant 5) and from a limiter further away toroidally (octant 2). While agreement was observed, e.g., for the top part of the IWGL on octant 2, notable differences between the experimental and simulation results were also found. For example, rather high deposition was observed in the central part of the limiter on octant 2, while ASCOT predictions indicated only minor ^{10}Be deposition there.

It is likely that matching these highly detailed measurements would require to consider the campaign-integrated nature of the experiment and the associated erosion of deposited ^{10}Be. However, the experimental results are in a very preliminary phase and no definite conclusions can be drawn before the completion of the studies. Forthcoming experimental results will also consider deposition in the divertor region, and modelling the experiment with the WallDyn [115, 116] (global migration over long time scales) and ERO (local migration) codes has been planned.

6. Conclusions and future prospects

The results presented in this thesis predict that the non-axisymmetric features in tokamaks influence global impurity transport in the SOL. In both ASDEX Upgrade and JET, the deposition patterns of tracer impurities simulated with the orbit-following ASCOT code were seen to strongly reflect the 3D features of the wall geometry, such as limiters. In particular on ASDEX Upgrade, this was shown to result in a toroidally asymmetric deposition pattern on the low-field side of the torus, in contrast to previous assumptions, which was also confirmed experimentally. These results highlighted the importance of a realistic wall geometry for impurity transport simulations in the SOL.

While the non-axisymmetric features of the magnetic field were predicted not to have a significant impact on impurity transport on a global scale, their influence was prominent when studying local-scale deposition. As both TF ripple and RMPs modify magnetic topology near the wall, the deposition patterns are determined by the connection of the 3D magnetic field with the 3D structures of the wall. Regarding reactor-scale devices, this suggests that reliable predictions of regions of high tritium retention cannot be obtained assuming axisymmetry.

Furthermore, it was observed that the impurity birth location in the far-SOL and halo plasma regions (far from the separatrix) can lead to deposition in the main chamber instead of the divertor region. Consequently, it is important to include the entire plasma between the separatrix and the wall in the analysis of global impurity migration.

According to the JET simulations, the limiter configuration can lead to long-range impurity transport within the main chamber. Similar scenarios will likely occur during the start-up and shutdown phases of discharges in ITER, and thus contribute to impurity migration besides the diverted plasma phases.

It should be observed that these results provide mainly an initial view of global impurity transport in a non-axisymmetric environment and serve as a basis for further studies. For more quantitative predictions, further development work should be conducted related to the simplifications used in the presented simulations.

Regarding the simulated particle transport, one potentially important aspect is that the collision operators in ASCOT do not account for the influence of parallel-B temperature gradients in the SOL. These gradients are typically small in the main chamber plasma and parallel-B transport is, therefore, dominated by plasma flow. More substantial gradients exist near the divertor region, however, which can reduce transport to the divertor. Furthermore, as electric fields were not included in the simulations, also the $\mathbf{E} \times \mathbf{B}$ drift was omitted. The presence of a radial electric field would arguably further influence the in-out asymmetry of divertor deposition as the $\mathbf{E}_r \times \mathbf{B}$ drift results in additional transport towards the outer divertor.

While these features can be implemented as part of neoclassical transport, accounting for turbulent transport is remarkably challenging. The use of a constant coefficient for anomalous radial diffusion in the presented simulations arguably provides an oversimplified model of radial impurity transport. If relying on a diffusion model, the diffusion coefficient $D_{\perp}^{\mathrm{imp}}$ should exhibit at least radial variation to express the experimentally observed substantially stronger radial transport in the far-SOL compared to the divertor-SOL, which increases main chamber deposition.

Additionally, impurity transport in the SOL is also strongly determined by the properties of the background plasma, in particular by plasma flow. In this work, the simulations utilised manually imposed plasma flow patterns with a constant Mach number in the main chamber. While this allowed more realistic predictions of tracer deposition, the poloidal and radial variations of the flow velocity cannot be disregarded in more quantitative studies. As the understanding of these variations is rather limited, however, the influence of the simplified flow pattern on the simulation results is difficult to quantify.

In a broader sense, a natural continuation of the work would be to extend the studies from transport to migration. The underlying assumption in the presented studies has been that especially in the case of tracer injection experiments, ASCOT transport simulations can provide valuable support to the experiments even when neglecting erosion. In the context

of reactor-relevant operation and a more detailed comparison to experimental results, however, accounting for the full migration chain is crucial and, for ASCOT, this would imply developing a plasma-surface interaction model for reflection and erosion of the followed particles. An alternative suggested way of creating a model for 3D impurity migration has been to employ ASCOT simulations as an input to the WallDyn code that self-consistently simulates the time evolution of the entire tokamak wall composition [117].

The amendment of ASCOT with respect to these simplifications would substantially increase the level of realism in the predictions and presents an important step when progressing towards more quantitative studies. Still, such work, e.g., for ITER would require also advances in the modelling of the background plasma, especially regarding the flows and extending the computational domain to the wall. Ideally, the non-axisymmetric nature of tokamaks should be considered also in modelling the background plasma, and input from 3D code packages such as EMC3-EIRENE could be utilised for ASCOT. This is important in particular regarding detailed studies of RMPs.

Moreover, the studies of this thesis mainly addressed L-mode plasmas with impurity sources in the main chamber. Regarding extrapolation of the results to high-performance tokamak operation, similar investigations could be performed also for H-mode conditions including the effects of ELMs, and for impurity sources at the divertor.

Besides tokamaks, commercial fusion energy is also pursued in parallel with the stellarator concept which exclusively relies on a carefully designed set of coils to create a confining magnetic field. While ITER operation is planned to begin only in the 2020s, the assembly of the leading stellarator device Wendelstein 7-X is already in its final stage with first plasmas planned for 2015 [118]. As stellarators are inherently strongly three-dimensional devices, the need for simulation codes such as ASCOT for investigating impurity migration is even more urgent than in tokamaks.

The results of this work therefore provide vast avenues for further research. In general, one of the main implications is that increased attention should be directed towards the non-axisymmetric features in tokamaks for a reliable assessment of impurity migration in reactor-scale devices.

Bibliography

[1] World Energy Council, *World Energy Scenarios: Composing energy futures to 2050*. World Energy Council, 2013.

[2] T. F. Stocker, D. Qin, G. K. Plattner, M. Tignor, S. K. Allen, J. Boschung, A. Nauels, Y. Xia, V. Bex, and P. M. Middgley, eds., *Climate Change 2013: The Physical Science Basis. Contribution of Working Group I to the Fifth Assessment Report of the Intergovernmental Panel on Climate Change*. Cambridge University Press, 2013.

[3] A. Glaser and R. J. Goldston, "Proliferation risks of magnetic fusion energy: clandestine production, covert production and breakout," *Nuclear Fusion*, vol. 52, p. 043004, 2012.

[4] G. Brumfiel, "Fusion's Missing Pieces," *Scientific American*, vol. 306, p. 56, 2012.

[5] K. Ikeda, "ITER on the road to fusion energy," *Nuclear Fusion*, vol. 50, p. 014002, 2010.

[6] J. Wesson, *Tokamaks*. Oxford University Press, 2004.

[7] J. D. Lawson, "Some Criteria for a Power Producing Thermonuclear Reactor," *Proceedings of the Physical Society. Section B*, vol. 70, p. 6, 1957.

[8] K. Ushigusa and JT-60 Team in *Fusion Energy, Proceedings of the 16th International Conference on Fusion Energy, Montreal, 1996, Volume 1*. p. 37.

[9] E. J. Doyle, W. A. Houlberg, Y. Kamada, V. Mukhovatov, T. H. Osborne, A. Polevoi, G. Bateman, J. W. Connor, J. G. Cordey, T. Fujita, X. Garbet, T. S. Hahm, L. D. Horton, A. E. Hubbard, F. Imbeaux, F. Jenko, J. E. Kinsey, Y. Kishimoto, J. Li, T. C. Luce, Y. Martin, M. Ossipenko, V. Parail, A. Peeters, T. L. Rhodes, J. E. Rice, C. M. Roach, V. Rozhansky, F. Ryter, G. Saibene, R. Sartori, A. C. C. Sips, J. A. Snipes, M. Sugihara, E. J. Synakowski, H. Takenaga, T. Takizuka, K. Thomsen, M. R. Wade, H. R. Wilson, ITPA Transport Physics Topical Group, ITPA Confinement Database and Modelling Topical Group, and ITPA Pedestal and Edge Topical Group, "Chapter 2: Plasma confinement and transport," *Nuclear Fusion*, vol. 47, p. S18, 2007. Progress in the ITER Physics Basis.

[10] F. Wagner, G. Becker, K. Behringer, D. Campbell, A. Eberhagen, W. Engelhardt, G. Fussmann, O. Gehre, J. Gernhardt, G. v. Gierke, G. Haas,

M. Huang, F. Karger, M. Keilhacker, O. Klüber, M. Kornherr, K. Lackner, G. Lisitano, G. G. Lister, H. M. Mayer, D. Meisel, E. R. Müller, H. Murmann, H. Niedermeyer, W. Poschenrieder, H. Rapp, H. Röhr, F. Schneider, G. Siller, E. Speth, A. Stäbler, K. H. Steuer, G. Venus, O. Vollmer, and Z. Yü, "Regime of Improved Confinement and High Beta in Neutral-Beam-Heated Divertor Discharges of the ASDEX Tokamak," *Physical Review Letters*, vol. 49, p. 1408, 1982.

[11] H. Zohm, "Edge localized modes (ELMs)," *Plasma Physics and Controlled Fusion*, vol. 38, p. 105, 1996.

[12] T. E. Evans, "ELM mitigation techniques," *Journal of Nuclear Materials*, vol. 438, Supplement, p. S11, 2013.

[13] R. J. Goldston, R. B. White, and A. H. Boozer, "Confinement of High-Energy Trapped Particles in Tokamaks," *Physical Review Letters*, vol. 47, p. 647, 1981.

[14] T. Kurki-Suonio, O. Asunta, T. Hellsten, V. Hynönen, T. Johnson, T. Koskela, J. Lönnroth, V. Parail, M. Roccella, G. Saibene, A. Salmi, and S. Sipilä, "ASCOT simulations of fast ion power loads to the plasma-facing components in ITER," *Nuclear Fusion*, vol. 49, p. 095001, 2009.

[15] S. Äkäslompolo, O. Asunta, T. Bergmans, M. Gagliardi, J. Galabert, E. Hirvijoki, T. Kurki-Suonio, S. Sipilä, A. Snicker, and K. Särkimäki, "Calculating the 3D magnetic field of ITER for European TBM studies," *Fusion Engineering and Design*. Submitted.

[16] T. E. Evans, R. A. Moyer, P. R. Thomas, J. G. Watkins, T. H. Osborne, J. A. Boedo, E. J. Doyle, M. E. Fenstermacher, K. H. Finken, R. J. Groebner, M. Groth, J. H. Harris, R. J. La Haye, C. J. Lasnier, S. Masuzaki, N. Ohyabu, D. G. Pretty, T. L. Rhodes, H. Reimerdes, D. L. Rudakov, M. J. Schaffer, G. Wang, and L. Zeng, "Suppression of Large Edge-Localized Modes in High-Confinement DIII-D Plasmas with a Stochastic Magnetic Boundary," *Physical Review Letters*, vol. 92, p. 235003, 2004.

[17] W. Suttrop, L. Barrera, A. Herrmann, R. M. McDermott, T. Eich, R. Fischer, B. Kurzan, P. T. Lang, A. Mlynek, T. Pütterich, S. K. Rathgeber, M. Rott, T. Vierle, E. Viezzer, M. Willensdorfer, E. Wolfrum, I. Zammuto, and the ASDEX Upgrade Team, "Studies of edge localized mode mitigation with new active in-vessel saddle coils in ASDEX Upgrade," *Plasma Physics and Controlled Fusion*, vol. 53, p. 124014, 2011.

[18] A. Loarte, G. Huijsmans, S. Futatani, L. R. Baylor, T. E. Evans, D. M. Orlov, O. Schmitz, M. Becoulet, P. Cahyna, Y. Gribov, A. Kavin, A. S. Naik, D. J. Campbell, T. Casper, E. Daly, H. Frerichs, A. Kischner, R. Laengner, S. Lisgo, R. A. Pitts, G. Saibene, and A. Wingen, "Progress on the application of ELM control schemes to ITER scenarios from the non-active phase to DT operation," *Nuclear Fusion*, vol. 54, p. 033007, 2014.

[19] T. E. Evans, R. K. W. Roeder, J. A. Carter, B. I. Rapoport, M. E. Fenstermacher, and C. J. Lasnier, "Experimental signatures of homoclinic tangles in poloidally diverted tokamaks," *Journal of Physics: Conference Series*, vol. 7, p. 174, 2005.

[20] M. W. Jakubowski, T. E. Evans, M. E. Fenstermacher, M. Groth, C. J. Lasnier, A. W. Leonard, O. Schmitz, J. G. Watkins, T. Eich, W. Fundamenski, R. A. Moyer, R. C. Wolf, L. B. Baylor, J. A. Boedo, K. H. Burrell, H. Frerichs, J. S. deGrassie, P. Gohil, I. Joseph, S. Mordijck, M. Lehnen, C. C. Petty, R. I. Pinsker, D. Reiter, T. L. Rhodes, U. Samm, M. J. Schaffer, P. B. Snyder, H. Stoschus, T. Osborne, B. Unterberg, E. Unterberg, and W. P. West, "Overview of the results on divertor heat loads in RMP controlled H-mode plasmas on DIII-D," *Nuclear Fusion*, vol. 49, p. 095013, 2009.

[21] O. Schmitz, T. E. Evans, M. E. Fenstermacher, A. McLean, J. Boedo, N. H. Brooks, H. Frerichs, M. Jakubowski, R. Laengner, C. L. Lasnier, A. Loarte, R. A. Moyer, D. Orlov, H. Reimerdes, D. Reiter, U. Samm, H. Stoschus, E. A. Unterberg, and J. G. Watkins, "The influence of three-dimensional stochastic magnetic boundaries on plasma edge transport and the resulting plasma wall interaction," *Journal of Nuclear Materials*, vol. 415, p. S886, 2011.

[22] L. A. Artsimovich, G. A. Brobrovskii, E. P. Gorbunov, D. P. Ivanov, V. D. Kirillov, E. I. Kuznetsov, S. V. Mirnov, M. P. Petrov, K. A. Rasumova, V. S. Strelkov, and D. A. Shcheglov in *Proceedings of the Third International Conference on Plasma Physics and Controlled Nuclear Fusion Research, Novosibirsk, 1968*. Paper CN24/B1.

[23] N. J. Peacock, D. C. Robinson, M. J. Forrest, P. D. Wilcock, and V. V. Sannikov, "Measurement of the Electron Temperature by Thomson Scattering in Tokamak T3," *Nature*, vol. 224, p. 488, 1969.

[24] P. C. Stangeby, *The Plasma Boundary of Magnetic Fusion Devices*. Plasma physics series, Institute of Physics Publishing, 2000.

[25] G. Federici, C. H. Skinner, J. N. Brooks, J. P. Coad, C. Grisolia, A. A. Haasz, A. Hassanein, V. Philipps, C. S. Pitcher, J. Roth, W. R. Wampler, and D. G. Whyte, "Plasma-material interactions in current tokamaks and their implications for next step fusion reactors," *Nuclear Fusion*, vol. 41, p. 1967, 2001.

[26] T. D. Burchell, "A microstructurally based fracture model for polygranular graphites," *Carbon*, vol. 34, p. 297, 1996.

[27] N. Taylor, S. Ciattaglia, P. Cortes, M. Iseli, S. Rosanvallon, and L. Topilski, "ITER safety and licensing update," *Fusion Engineering and Design*, vol. 87, p. 476, 2012.

[28] A. Loarte, B. Lipschultz, A. S. Kukushkin, G. F. Matthews, P. C. Stangeby, N. Asakura, G. F. Counsell, G. Federici, A. Kallenbach, K. Krieger, A. Mahdavi, V. Philipps, D. Reiter, J. Roth, J. Strachan, D. Whyte, R. Doerner, T. Eich, W. Fundamenski, A. Herrmann, M. Fenstermacher, P. Ghendrih, M. Groth, A. Kirschner, S. Konoshima, B. LaBombard, P. Lang, A. W. Leonard, P. Monier-Garbet, R. Neu, H. Pacher, B. Pegourie, R. A. Pitts, S. Takamura, J. Terry, E. Tsitrone, and the ITPA Scrape-off Layer and Divertor Physics Topical Group, "Chapter 4: Power and particle control," *Nuclear Fusion*, vol. 47, p. S203, 2007. Progress in the ITER Physics Basis.

[29] R. A. Pitts, S. Carpentier, F. Escourbiac, T. Hirai, V. Komarov, S. Lisgo, A. S. Kukushkin, A. Loarte, M. Merola, A. S. Naik, R. Mitteau, M. Sugihara, B. Bazylev, and P. C. Stangeby, "A full tungsten divertor for ITER:

Physics issues and design status," *Journal of Nuclear Materials*, vol. 438, Supplement, p. S48, 2013.

[30] G. F. Matthews, M. Beurskens, S. Brezinsek, M. Groth, E. Joffrin, A. Loving, M. Kear, M.-L. Mayoral, R. Neu, P. Prior, V. Riccardo, F. Rimini, M. Rubel, G. Sips, E. Villedieu, P. de Vries, M. L. Watkins, and EFDA-JET contributors, "JET ITER-like wall – overview and experimental programme," *Physica Scripta*, no. T145, p. 014001, 2011.

[31] R. P. Doerner, M. J. Baldwin, and R. A. Causey, "Beryllium-tungsten mixed-material interactions," *Journal of Nuclear Materials*, vol. 342, p. 63, 2005.

[32] J. Roth, R. Preuss, W. Bohmeyer, S. Brezinsek, A. Cambe, E. Casarotto, R. Doerner, E. Gauthier, G. Federici, S. Higashijima, J. Hogan, A. Kallenbach, A. Kirschner, H. Kubo, J. M. Layet, T. Nakano, V. Philipps, A. Pospieszczyk, R. Pugno, R. Ruggiéri, B. Schweer, G. Sergienko, and M. Stamp, "Flux dependence of carbon chemical erosion by deuterium ions," *Nuclear Fusion*, vol. 44, p. L21, 2004.

[33] N. Asakura and ITPA SOL and Divertor Topical Group, "Understanding the SOL flow in L-mode plasma on divertor tokamaks, and its influence on the plasma transport," *Journal of Nuclear Materials*, vol. 363–365, p. 41, 2007.

[34] B. Lipschultz, X. Bonnin, G. Counsell, A. Kallenbach, A. Kukushkin, K. Krieger, A. Leonard, A. Loarte, R. Neu, R. Pitts, T. Rognlien, J. Roth, C. Skinner, J. L. Terry, E. Tsitrone, D. Whyte, S. Zweben, N. Asakura, D. Coster, R. Doerner, R. Dux, G. Federici, M. Fenstermacher, W. Fundamenski, P. Ghendrih, A. Herrmann, J. Hu, S. Krasheninnikov, G. Kirnev, A. Kreter, V. Kurnaev, B. LaBombard, S. Lisgo, T. Nakano, N. Ohno, H. D. Pacher, J. Paley, Y. Pan, G. Pautasso, V. Philipps, V. Rohde, D. Rudakov, P. Stangeby, S. Takamura, T. Tanabe, Y. Yang, and S. Zhu, "Plasma-surface interaction, scrape-off layer and divertor physics: implications for ITER," *Nuclear Fusion*, vol. 47, p. 1189, 2007.

[35] R. A. Pitts, J. P. Coad, D. P. Coster, G. Federici, W. Fundamenski, J. Horacek, K. Krieger, A. Kukushkin, J. Likonen, G. F. Matthews, M. Rubel, J. D. Strachan, and JET-EFDA contributors, "Material erosion and migration in tokamaks," *Plasma Physics and Controlled Fusion*, vol. 47, p. B303, 2005.

[36] P. C. Stangeby, "Assessing material migration through ^{13}C injection experiments," *Journal of Nuclear Materials*, vol. 415, p. S278, 2011.

[37] R. Neu, C. Hopf, A. Kallenbach, T. Pütterich, R. Dux, H. Greuner, O. Gruber, A. Herrmann, K. Krieger, H. Maier, V. Rohde, and ASDEX Upgrade Team, "Operational conditions in a W-clad tokamak," *Journal of Nuclear Materials*, vol. 367–370, Part B, p. 1497, 2007.

[38] I. Zolle, *Technetium-99m Pharmaceuticals: Preparation and Quality Control in Nuclear Medicine*. Springer, 2007.

[39] C. C. Ebbesmeyer and W. J. Ingraham, "Pacific toy spill fuels ocean current pathways research," *Eos, Transactions American Geophysical Union*, vol. 75, p. 425, 1994.

[40] U. Kögler, F. Weschenfelder, J. Winter, H. G. Esser, V. Philipps, A. Pospieszczyk, B. Schweer, J. Von Seggern, M. Z. Tokar, and P. Wienhold, "Studies on plasma edge transport and layer deposition by local injection of reactive gases during TEXTOR-94 discharges," *Journal of Nuclear Materials*, vol. 241–243, p. 816, 1997.

[41] D. S. McPhail, "Applications of Secondary Ion Mass Spectrometry (SIMS) in Materials Science," *Journal of Materials Science*, vol. 41, p. 873, 2006.

[42] M. Berglund and M. E. Wieser, "Isotopic compositions of the elements 2009 (IUPAC Technical Report)," *Pure and Applied Chemistry*, vol. 83, p. 397, 2011.

[43] J. Likonen, S. Lehto, J. P. Coad, T. Renvall, T. Sajavaara, T. Ahlgren, D. E. Hole, G. F. Matthews, and J. Keinonen, "Studies of impurity deposition/implantation in JET divertor tiles using SIMS and ion beam techniques," *Fusion Engineering and Design*, vol. 66–68, p. 219, 2003.

[44] J. P. Coad, J. Likonen, M. Rubel, E. Vainonen-Ahlgren, D. E. Hole, T. Sajavaara, T. Renvall, G. F. Matthews, and JET EFDA Contributors, "Overview of material re-deposition and fuel retention studies at JET with the Gas Box divertor," *Nuclear Fusion*, vol. 46, p. 350, 2006.

[45] R. Pugno, K. Krieger, A. Kirschner, A. Kallenbach, D. P. Coster, R. Dux, U. Fantz, J. Likonen, H. W. Müller, J. Neuhauser, V. Rohde, E. Vainonen-Ahlgren, and ASDEX Upgrade Team, "Carbon chemical erosion in H-mode discharges in ASDEX Upgrade divertor IIb: flux dependence and local redeposition," *Journal of Nuclear Materials*, vol. 337–339, p. 985, 2005.

[46] A. Hakola, J. Likonen, L. Aho-Mantila, M. Groth, S. Koivuranta, K. Krieger, T. Kurki-Suonio, T. Makkonen, M. Mayer, H. W. Müller, R. Neu, V. Rohde, and the ASDEX Upgrade Team, "Migration and deposition of ^{13}C in the full-tungsten ASDEX Upgrade tokamak," *Plasma Physics and Controlled Fusion*, vol. 52, p. 065006, 2010.

[47] S. L. Allen, W. R. Wampler, A. G. McLean, D. G. Whyte, W. P. West, P. C. Stangeby, N. H. Brooks, D. L. Rudakov, V. Phillips, M. Rubel, G. F. Matthews, A. Nagy, R. Ellis, and A. S. Bozek, "^{13}C transport studies in L-mode divertor plasmas on DIII-D," *Journal of Nuclear Materials*, vol. 337–339, p. 30, 2005.

[48] W. R. Wampler, A. G. McLean, S. L. Allen, N. H. Brooks, J. D. Elder, M. E. Fenstermacher, M. Groth, P. C. Stangeby, W. P. West, and D. G. Whyte, "Transport and deposition of ^{13}C from methane injection into partially detached H-mode plasmas in DIII-D," *Journal of Nuclear Materials*, vol. 363–365, p. 72, 2007.

[49] Y. Ueda, M. Fukumoto, J. Watanabe, Y. Ohtsuka, T. Arai, N. Asakura, Y. Nobuta, M. Sato, T. Nakano, J. Yagyu, K. Ochiai, K. Takakura, T. Tanabe, and the JT-60 Team, "Localized tungsten deposition in divertor region in JT-60U," *Nuclear Fusion*, vol. 49, p. 065027, 2009.

[50] P. Wienhold, H. G. Esser, D. Hildebrandt, A. Kirschner, M. Mayer, V. Philipps, and M. Rubel, "Investigation of carbon transport in the scrape-off layer of TEXTOR-94," *Journal of Nuclear Materials*, vol. 290–293, p. 362, 2001.

[51] A. Kreter, D. Borodin, S. Brezinsek, S. Droste, T. Hirai, A. Kirschner, A. Litnovsky, M. Mayer, V. Philipps, A. Pospieszczyk, Y. Sakawa, U. Samm, O. Schmitz, G. Sergienko, T. Tanabe, Y. Ueda, P. Wienhold, and the TEXTOR Team, "Investigation of carbon transport by $^{13}CH_4$ injection through graphite and tungsten test limiters in TEXTOR," *Plasma Physics and Controlled Fusion*, vol. 48, p. 1401, 2006.

[52] A. Kirschner, A. Kreter, P. Wienhold, S. Brezinsek, J. W. Coenen, H. G. Esser, A. Pospieszczyk, C. Schulz, U. Breuer, D. Borodin, M. Clever, R. Ding, A. Galonska, A. Huber, A. Litnovsky, D. Matveev, K. Ohya, V. Philipps, U. Samm, O. Schmitz, B. Schweer, H. Stoschus, and TEXTOR Team, "Deposition and re-erosion studies by means of local impurity injection in TEXTOR," *Journal of Nuclear Materials*, vol. 415, Supplement, p. S239, 2011.

[53] P. Petersson, A. Hakola, J. Likonen, M. Mayer, J. Miettunen, R. Neu, V. Rohde, M. Rubel, and the ASDEX-Upgrade Team, "Injection of nitrogen-15 tracer into ASDEX-Upgrade: New technique in material migration studies," *Journal of Nuclear Materials*, vol. 438, Supplement, p. S616, 2013.

[54] L. Aho-Mantila, M. Wischmeier, H. W. Müller, S. Potzel, D. Coster, X. Bonnin, G. D. Conway, and the ASDEX Upgrade Team, "Outer divertor of ASDEX Upgrade in low-density L-mode discharges in forward and reversed magnetic field: I. Comparison between measured plasma conditions and SOLPS5.0 code calculations," *Nuclear Fusion*, vol. 52, p. 103006, 2012.

[55] L. Aho-Mantila, M. Wischmeier, K. Krieger, V. Rohde, A. Hakola, S. Potzel, A. Kirschner, D. Borodin, and the ASDEX Upgrade Team, "Outer divertor of ASDEX upgrade in low-density L-mode discharges in forward and reversed magnetic field: II. Analysis of local impurity migration," *Nuclear Fusion*, vol. 52, p. 103007, 2012.

[56] A. Hakola, M. I. Airila, C. Björkas, D. Borodin, S. Brezinsek, J. P. Coad, M. Groth, A. Järvinen, A. Kirschner, S. Koivuranta, K. Krieger, T. Kurki-Suonio, J. Likonen, V. Lindholm, T. Makkonen, M. Mayer, J. Miettunen, H. W. Müller, R. Neu, P. Petersson, V. Rohde, M. Rubel, A. Widdowson, the ASDEX Upgrade Team, and JET-EFDA Contributors, "Global migration of impurities in tokamaks," *Plasma Physics and Controlled Fusion*, vol. 55, p. 124029, 2013.

[57] A. Hakola, S. Koivuranta, J. Likonen, M. Groth, T. Kurki-Suonio, V. Lindholm, J. Miettunen, K. Krieger, M. Mayer, H. W. Müller, R. Neu, V. Rohde, P. Petersson, and ASDEX Upgrade Team, "Global migration of ^{13}C impurities in high-density L-mode plasmas in ASDEX Upgrade," *Journal of Nuclear Materials*, vol. 438, Supplement, p. S694, 2013.

[58] A. Kallenbach, R. Dux, J. C. Fuchs, R. Fischer, B. Geiger, L. Giannone, A. Herrmann, T. Lunt, V. Mertens, R. McDermott, R. Neu, T. Pütterich, S. Rathgeber, V. Rohde, K. Schmid, J. Schweinzer, W. Treutterer, and ASDEX Upgrade Team, "Divertor power load feedback with nitrogen seeding in ASDEX Upgrade," *Plasma Physics and Controlled Fusion*, vol. 52, p. 055002, 2010.

[59] P. Petersson, M. Rubel, G. Possnert, S. Brezinsek, A. Kreter, S. Möller, A. Hakola, M. Mayer, M. I. Airila, T. Makkonen, J. Miettunen, R. Neu,

V. Rohde, the TEXTOR Team, and the ASDEX Upgrade Team, "Overview of Nitrogen-15 application as a tracer gas for material migration and retention studies in tokamaks," *Physica Scripta*, vol. T159, 2014.

[60] A. S. Kukushkin, H. D. Pacher, and R. A. Pitts, "Characteristics of divertor detachment for ITER conditions," *Journal of Nuclear Materials*, 2014. Accepted, doi:10.1016/j.jnucmat.2014.10.042.

[61] K. Krieger, A. Geier, X. Gong, H. Maier, R. Neu, V. Rohde, and the ASDEX Upgrade Team, "Erosion and migration of tungsten employed at the main chamber first wall of ASDEX Upgrade," *Journal of Nuclear Materials*, vol. 313–316, p. 327, 2003.

[62] K. Krieger, J. Likonen, M. Mayer, R. Pugno, V. Rohde, E. Vainonen-Ahlgren, and ASDEX Upgrade Team, "Tungsten redistribution patterns in ASDEX Upgrade," *Journal of Nuclear Materials*, vol. 337–339, p. 10, 2005.

[63] H. Bergsåker, G. Possnert, I. Bykov, K. Heinola, P. Petersson, J. Miettunen, A. Widdowson, V. Riccardo, I. Nunes, M. Stamp, S. Brezinsek, M. Groth, T. Kurki-Suonio, J. Likonen, J. P. Coad, D. Borodin, A. Kirschner, K. Schmid, K. Krieger, and JET EFDA Contributors, "First results from the ^{10}Be marker experiment in JET with ITER-like wall," *Nuclear Fusion*, vol. 54, p. 082004, 2014.

[64] J. C. Gosse and F. M. Phillips, "Terrestrial in situ cosmogenic nuclides: theory and application," *Quaternary Science Reviews*, vol. 20, p. 1475, 2001.

[65] F. Leipziger, "Some New Upper Limits of Isotopic Abundance By Mass Spectrometry," *Applied Spectroscopy*, vol. 17, p. 158, 1963.

[66] A. Aldahan and G. Possnert, "Geomagnetic and climatic variability reflected by ^{10}Be during the Quaternary and late Pliocene," *Geophysical Research Letters*, vol. 30, p. 3401, 2003.

[67] R. Schneider, X. Bonnin, K. Borrass, D. P. Coster, H. Kastelewicz, D. Reiter, V. A. Rozhansky, and B. J. Braams, "Plasma Edge Physics with B2-Eirene," *Contributions to Plasma Physics*, vol. 46, p. 3, 2006.

[68] A. Taroni, G. Corrigan, G. Radford, R. Simonini, J. Spence, and S. Weber, "The Multi-Fluid Codes EDGE1D and EDGE2D: Models and Results," *Contributions to Plasma Physics*, vol. 32, p. 438, 1992.

[69] D. Reiter, "Progress in two-dimensional plasma edge modelling," *Journal of Nuclear Materials*, vol. 196–198, p. 80, 1992.

[70] S. I. Braginskii, "Transport Processes in a Plasma," *Reviews of Plasma Physics*, vol. 1, 1965.

[71] M. Wischmeier, M. Groth, S. Wiesen, S. Potzel, L. Aho-Mantila, D. P. Coster, R. Dux, C. Fuchs, A. Kallenbach, H. W. Müller, D. Reiter, A. Scarabosio, and the ASDEX Upgrade Team, "Assessment of edge modeling in support of ITER," *Journal of Nuclear Materials*, vol. 415, Supplement, p. S523, 2011.

[72] S. K. Erents, R. A. Pitts, W. Fundamenski, J. P. Gunn, and G. F. Matthews, "A comparison of experimental measurements and code results to determine flows in the JET SOL," *Plasma Physics and Controlled Fusion*, vol. 46, p. 1757, 2004.

[73] M. Groth, J. A. Boedo, N. H. Brooks, R. C. Isler, A. W. Leonard, G. D. Porter, J. G. Watkins, W. P. West, B. D. Bray, M. E. Fenstermacher, R. J. Groebner, R. A. Moyer, D. L. Rudakov, J. H. Yu, and L. Zeng, "Effect of cross-field drifts on flows in the main scrape-off-layer of DIII-D L-mode plasmas," *Nuclear Fusion*, vol. 49, p. 115002, 2009.

[74] D. P. Coster, X. Bonnin, A. Chankin, G. Corrigan, S. K. Erents, W. Fundamenski, J. Hogan, A. Huber, A. Kallenbach, G. Kirnev, A. Kirschner, T. Kiviniemi, S. Kuhn, A. Loarte, J. Lönnroth, G. F. Matthews, R. A. Pitts, S. Sipilä, J. Spence, J. Strachan, F. Subba, E. Tsitrone, D. Tskhakaya, S. Wiesen, M. Warrier, M. Wischmeier, R. Zanino, and contributors to the EFDA-JET work programme in *Proceedings of the 20th IAEA Fusion Energy Conference (Vilamoura, Portugal)*, 2004. Paper IAEA-CN-116/TH/P5-18.

[75] A. V. Chankin, D. P. Coster, N. Asakura, X. Bonnin, G. D. Conway, G. Corrigan, S. K. Erents, W. Fundamenski, J. Horacek, A. Kallenbach, M. Kaufmann, C. Konz, K. Lackner, H. W. Müller, J. Neuhauser, R. A. Pitts, and M. Wischmeier, "Discrepancy between modelled and measured radial electric fields in the scrape-off layer of divertor tokamaks: A challenge for 2D fluid codes?," *Nuclear Fusion*, vol. 47, p. 479, 2007.

[76] A. V. Chankin, D. P. Coster, N. Asakura, G. Corrigan, S. K. Erents, W. Fundamenski, H. W. Müller, R. A. Pitts, P. C. Stangeby, and M. Wischmeier, "A possible role of radial electric field in driving parallel ion flow in scrape-off layer of divertor tokamaks," *Nuclear Fusion*, vol. 47, p. 762, 2007.

[77] T. Takizuka, K. Shimizu, N. Hayashi, M. Hosokawa, and M. Yagi, "Two-dimensional full particle simulation of the flow patterns in the scrape-off-layer plasma for upper- and lower-null point divertor configurations in tokamaks," *Nuclear Fusion*, vol. 49, p. 075038, 2009.

[78] A. G. McLean, J. D. Elder, P. C. Stangeby, S. L. Allen, J. A. Boedo, N. H. Brooks, M. E. Fenstermacher, M. Groth, S. Lisgo, A. Nagy, D. L. Rudakov, W. R. Wampler, J. G. Watkins, W. P. West, and D. G. Whyte, "DIVIMP modeling of the toroidally symmetrical injection of $^{13}CH_4$ into the upper SOL of DIII-D," *Journal of Nuclear Materials*, vol. 337-339, p. 124, 2005.

[79] J. D. Elder, A. G. McLean, P. C. Stangeby, S. L. Allen, J. A. Boedo, B. D. Bray, N. H. Brooks, M. E. Fenstermacher, M. Groth, A. W. Leonard, D. Reiter, D. L. Rudakov, W. R. Wampler, J. G. Watkins, W. P. West, and D. G. Whyte, "OEDGE modeling of the DIII-D H-mode $^{13}CH_4$ puffing experiment," *Journal of Nuclear Materials*, vol. 363-365, p. 140, 2007.

[80] T. Makkonen, M. Groth, T. Kurki-Suonio, K. Krieger, L. Aho-Mantila, A. Hakola, J. Likonen, H. W. Müller, and the ASDEX Upgrade Team, "DIVIMP simulations of ^{13}C puffing experiments in ASDEX Upgrade L-mode plasma," *Journal of Nuclear Materials*, vol. 415, Supplement, p. S479, 2011.

[81] A. Kirschner, V. Philipps, J. Winter, and U. Kögler, "Simulation of the plasma-wall interaction in a tokamak with the Monte Carlo code ERO-TEXTOR," *Nuclear Fusion*, vol. 40, p. 989, 2000.

[82] U. Kögler and J. Winter, "ERO-TEXTOR: 3D-Monte-Carlo Code for Local Impurity Modeling in the Scrape-Off-Layer of TEXTOR," 1997. Report Jül-3361, Forschungszentrum Jülich, ISSN 0944-2952.

[83] A. Snicker, T. Kurki-Suonio, and S. Sipilä, "Realistic Simulations of Fast-Ion Wall Distribution Including Effects Due to Finite Larmor Radius," *IEEE Transactions on Plasma Science*, vol. 38, p. 2177, 2010.

[84] F. L. Hinton and R. D. Hazeltine, "Theory of plasma transport in toroidal confinement systems," *Reviews Modern Physics*, vol. 48, p. 239, 1976.

[85] A. J. Wootton, M. E. Austin, R. D. Bengtson, J. A. Boedo, R. V. Bravenec, D. L. Brower, J. Y. Chen, G. Cima, P. H. Diamond, R. D. Durst, P. H. Edmonds, S. P. Fan, M. S. Foster, J. C. Forster, R. Gandy, K. W. Gentle, R. L. Hickok, Y. X. Hey, S. K. Kim, Y. J. Kim, H. Lin, N. C. Luhmann, S. C. McCool, W. H. Miner, A. Ouroua, D. M. Patterson, W. A. Peebles, P. E. Phillips, B. Richards, C. P. Ritz, T. L. Rhodes, D. W. Ross, W. L. Rowan, P. M. Schoch, D. Sing, E. J. Synakowski, P. W. Terry, K. W. Wenzel, J. C. Wiley, X. Z. Yang, X. H. Yu, Z. Zhang, and S. B. Zheng, "Fluctuations and anomalous transport (in tokamaks, particularly TEXT)," *Plasma Physics and Controlled Fusion*, vol. 30, p. 1479, 1988.

[86] S. Sipilä, *Simulation of Charged Particle Orbits in a Tokamak*. Licentiate thesis, Helsinki University of Technology, 1993.

[87] E. Hirvijoki, O. Asunta, T. Koskela, T. Kurki-Suonio, J. Miettunen, S. Sipilä, A. Snicker, and S. Äkäslompolo, "ASCOT: Solving the kinetic equation of minority particle species in tokamak plasmas," *Computer Physics Communications*, vol. 185, p. 1310, 2014.

[88] T. Kurki-Suonio, O. Asunta, E. Hirvijoki, T. Koskela, A. Snicker, T. Hauff, F. Jenko, E. Poli, and S. Sipilä, "Fast ion power loads on ITER first wall structures in the presence of NTMs and microturbulence," *Nuclear Fusion*, vol. 51, p. 083041, 2011.

[89] A. Snicker, S. Sipilä, and T. Kurki-Suonio, "Orbit-following fusion alpha wall load simulation for ITER scenario 4 including full orbit effects," *Nuclear Fusion*, vol. 52, p. 094011, 2012.

[90] A. Snicker, E. Hirvijoki, and T. Kurki-Suonio, "Power loads to ITER first wall structures due to fusion alphas in a non-axisymmetric magnetic field including the presence of MHD modes," *Nuclear Fusion*, vol. 53, p. 093028, 2013.

[91] P. C. Stangeby, C. Farrell, S. Hoskins, and L. Wood, "Monte Carlo modelling of impurity ion transport for a limiter source/sink," *Nuclear Fusion*, vol. 28, p. 1945, 1988.

[92] P. C. Stangeby and J. D. Elder, "Calculation of observable quantities using a divertor impurity interpretive code, DIVIMP," *Journal of Nuclear Materials*, vol. 196, p. 258, 1992.

[93] A. H. Boozer and G. Kuo-Petravic, "Monte Carlo evaluation of transport coefficients," *Physics of Fluids*, vol. 24, p. 851, 1981.

[94] D. Reiser, D. Reiter, and M. Tokar, "Improved kinetic test particle model for impurity transport in tokamaks," *Nuclear Fusion*, vol. 38, p. 165, 1998.

[95] T. Hauff, M. J. Pueschel, T. Dannert, and F. Jenko, "Electrostatic and magnetic transport of energetic ions in turbulent plasmas," *Physical Review Letters*, vol. 102, p. 075004, 2009.

[96] H. P. Summers, "The ADAS User Manual, version 2.6." http://www.adas.ac.uk, 2004.

[97] P. J. McCarthy, "Analytical solutions to the Grad–Shafranov equation for tokamak equilibrium with dissimilar source functions," *Physics of Plasmas*, vol. 6, p. 3554, 1999.

[98] L. L. Lao, H. S. John, R. D. Stambaugh, A. G. Kellman, and W. Pfeiffer, "Reconstruction of current profile parameters and plasma shapes in tokamaks," *Nuclear Fusion*, vol. 25, p. 1611, 1985.

[99] Y. Liu, A. Kirk, Y. Gribov, M. P. Gryaznevich, T. C. Hender, and E. Nardon, "Modelling of plasma response to resonant magnetic perturbation fields in MAST and ITER," *Nuclear Fusion*, vol. 51, p. 083002, 2011.

[100] H. J. Klingshirn, D. P. Coster, and X. Bonnin, "Advanced spatial discretizations in the B2.5 plasma fluid code," *Journal of Nuclear Materials*, vol. 438, Supplement, p. S856, 2013.

[101] D. L. Rudakov, J. A. Boedo, R. A. Moyer, P. C. Stangeby, J. G. Watkins, D. G. Whyte, L. Zeng, N. H. Brooks, R. P. Doerner, T. E. Evans, M. E. Fenstermacher, M. Groth, E. M. Hollmann, S. I. Krasheninnikov, C. J. Lasnier, A. W. Leonard, M. A. Mahdavi, G. R. McKee, A. G. McLean, A. Y. Pigarov, W. R. Wampler, G. Wang, W. P. West, and C. P. C. Wong, "Far SOL transport and main wall plasma interaction in DIII-D," *Nuclear Fusion*, vol. 45, p. 1589, 2005.

[102] S. Äkäslompolo, T. Koskela, T. Kurki-Suonio, T. Lunt, J. Miettunen, and E. Hirvijoki, "Preparing tokamak 3D wall and magnetic data for particle tracing simulations," *Europhysics Conference Abstracts*, vol. 36F, p. P5.058, 2012. 39th European Physical Society Conference on Plasma Physics.

[103] B. LaBombard, M. Umansky, R. Boivin, J. Goetz, J. Hughes, B. Lipschultz, D. Mossessian, C. Pitcher, J. Terry, and Alcator Group, "Cross-field plasma transport and main-chamber recycling in diverted plasmas on Alcator C-Mod," *Nuclear Fusion*, vol. 40, p. 2041, 2000.

[104] K. Schmid, A. Manhard, C. Linsmeier, A. Wiltner, T. Schwarz-Selinger, W. Jacob, and S. Mändl, "Interaction of nitrogen plasmas with tungsten," *Nuclear Fusion*, vol. 50, p. 025006, 2010.

[105] G. Meisl, K. Schmid, M. Oberkofler, K. Krieger, S. W. Lisgo, L. Aho-Mantila, F. Reimold, and the ASDEX Upgrade Team, "Nitrogen retention in ASDEX Upgrade," *Journal of Nuclear Materials*, 2014. Accepted, 10.1016/j.jnucmat.2014.10.031.

[106] O. Schmitz, T. E. Evans, M. E. Fenstermacher, H. Frerichs, M. W. Jakubowski, M. J. Schaffer, A. Wingen, W. P. West, N. H. Brooks, K. H. Burrell, J. S. deGrassie, Y. Feng, K. H. Finken, P. Gohil, M. Groth, I. Joseph, C. J. Lasnier, M. Lehnen, A. W. Leonard, S. Mordijck, R. A. Moyer, A. Nicolai, T. H. Osborne, D. Reiter, U. Samm, K. H. Spatschek, H. Stoschus, B. Unterberg, E. A. Unterberg, J. G. Watkins, R. Wolf, and the DIII-D and TEXTOR Teams, "Aspects of three dimensional transport for ELM control experiments in ITER-similar shape plasmas at low collisionality in DIII-D," *Plasma Physics and Controlled Fusion*, vol. 50, p. 124029, 2008.

[107] H. Frerichs, D. Reiter, O. Schmitz, T. E. Evans, and Y. Feng, "Three-dimensional edge transport simulations for DIII-D plasmas with resonant magnetic perturbations," *Nuclear Fusion*, vol. 50, p. 034004, 2010.

[108] T. Lunt, Y. Feng, M. Bernert, A. Herrmann, P. de Marné, R. McDermott, H. W. Müller, S. Potzel, T. Pütterich, S. Rathgeber, W. Suttrop, E. Viezzer, E. Wolfrum, M. Willensdorfer, and the ASDEX Upgrade team, "First EMC3-Eirene simulations of the impact of the edge magnetic perturbations at ASDEX Upgrade compared with the experiment," *Nuclear Fusion*, vol. 52, p. 054013, 2012.

[109] Y. Feng, F. Sardei, J. Kisslinger, P. Grigull, K. McCormick, and D. Reiter, "3D Edge Modeling and Island Divertor Physics," *Contributions to Plasma Physics*, vol. 44, p. 57, 2004.

[110] C. Silva, G. Arnoux, S. Devaux, D. Frigione, M. Groth, J. Horacek, P. J. Lomas, S. Marsen, G. Matthews, and R. A. Pitts, "Comparison of scrape-off layer transport in inner and outer wall limited JET plasmas," *Journal of Nuclear Materials*, vol. 438, Supplement, p. S189, 2013.

[111] M. Groth, P. Belo, S. Brezinsek, M. Brix, J. W. Coenen, C. Corrigan, J. Flanagan, D. Harting, A. Huber, S. Jachmich, A. Järvinen, U. Kruezi, M. Lehnen, C. Lowry, A. G. Meigs, S. Marsen, S. Munaretto, M. F. Stamp, and JET EFDA Contributors, "Divertor plasma and neutral conditions in JET-ILW ohmic plasmas in semi-horizontal and vertical divertor configurations," *Europhysics Conference Abstracts*, vol. 37D, p. P1.115, 2013. 40th European Physical Society Conference on Plasma Physics.

[112] J. P. Coad, S. Gruenhagen, D. E. Hole, A. Hakola, S. Koivuranta, J. Likonen, M. Rubel, A. Widdowson, and JET-EFDA contributors, "Overview of JET post-mortem results following the 2007–9 operational period, and comparisons with previous campaigns," *Physica Scripta*, no. T145, p. 014003, 2011.

[113] J. P. Coad, Culham Centre for Fusion Energy. Private communications, 2012.

[114] I. Bykov, H. Bergsåker, G. Possnert, K. Heinola, J. Miettunen, M. Groth, P. Petersson, A. Widdowson, J. Likonen, and JET EFDA contributors, "Materials migration in JET with ITER-like wall traced with a ^{10}Be isotopic marker," *Journal of Nuclear Materials*, 2014. Accepted, doi:10.1016/j.jnucmat.2014.12.020.

[115] K. Schmid, M. Reinelt, and K. Krieger, "An integrated model of impurity migration and wall composition dynamics for tokamaks," *Journal of Nuclear Materials*, vol. 415, Supplement, p. S284, 2011.

[116] K. Schmid, “Implementation of a diffusion convection surface evolution model in WallDYN,” *Journal of Nuclear Materials*, vol. 438, Supplement, p. S484, 2013.

[117] K. Schmid, Max-Planck-Institut für Plasmaphysik. Private communications, 2014.

[118] M. Gasparotto, C. Baylard, H.-S. Bosch, D. Hartmann, T. Klinger, R. Vilbrandt, and L. Wegener, “Wendelstein 7-X – Status of the project and commissioning planning,” *Fusion Engineering and Design*, vol. 89, p. 2121, 2014.

Aalto-DD 61/2015

As the need for clean, safe and abundant sources of energy is ever increasing, research on *fusion energy* is progressing towards reactor-scale devices. A key challenge for magnetic confinement fusion devices such as *tokamaks* is the interaction of the hot plasma fuel with the surrounding wall surfaces, leading to generation of *impurities* that migrate in the plasma. Understanding of impurity migration is crucial for the successful operation of future reactors.

This thesis presents simulations of transport of tracer impurities in the ASDEX Upgrade and JET tokamaks, addressing experiments conducted on these devices. In particular, the influence of *non-axisymmetric* (3D) features of the wall geometry and magnetic field on impurity transport is investigated. The studies have substantially aided the interpretation of the experimental results and suggest that the 3D features should not be disregarded when making quantitative predictions of impurity migration in next-step devices.

ISBN 978-952-60-6189-4 (printed)
ISBN 978-952-60-6190-0 (pdf)
ISSN-L 1799-4934
ISSN 1799-4934 (printed)
ISSN 1799-4942 (pdf)

Aalto University
School of Science
Department of Applied Physics
www.aalto.fi

BUSINESS + ECONOMY

ART + DESIGN + ARCHITECTURE

SCIENCE + TECHNOLOGY

CROSSOVER

DOCTORAL DISSERTATIONS